

# Exploring Leaky Modes in the Subducted Pacific Plate



Jonathan Simpson  
Department of Physics  
The University of Auckland

Supervisor: Dr. Kasper van Wijk

A dissertation submitted in partial fulfilment of the requirements for the degree of BSc(Hons)  
in Geophysics, The University of Auckland, 2017.



# Abstract

Anomalous dispersion of seismic waves propagating through subduction zones is observed around the world. In New Zealand, earthquakes with epicentres in the Kermadec subduction zone to the North are often recorded with low amplitude high-frequency ( $> 3$  Hz) precursors preceding the arrival of lower frequency energy by up to 10 seconds. Previous studies have shown that this energy travels through a continuous thin high velocity layer within the subducted slab which permits the propagation of only certain high-frequency waves, known as “leaky modes”. Using data from eight seismometers in the GeoNet network along the East Coast of New Zealand, this study examines the arrival times and frequency content of these high-frequency precursors. For a catalogue of 97 earthquakes, the seismograms at each station are examined for the presence of a precursor, showing that a high-frequency arrival is observed at one or more stations for 53 of the events. The most number of precursors are observed at a station in the lower North Island, while the least number of precursors are observed at stations in the South Island. No strong relationship is found between the epicentre location and the station at which a precursor is first observed. An explanation for the variability in the occurrence of precursors at different stations within New Zealand is presented, proposing that the location of ray paths with respect to the high velocity layer, along with the velocity structure and location of the subducted Hikurangi slab beneath New Zealand, are factors which may influence the propagation of the leaky modes to stations in New Zealand. This explanation is consistent with the distribution in the occurrence of precursors at the seismometer stations.



# Contents

<b>Abstract</b>	<b>1</b>
<b>1 Introduction</b>	<b>7</b>
1.0.1 Dispersion in Subduction Zone Earthquakes . . . . .	7
1.0.2 Mathematical Description of Leaky Modes . . . . .	10
<b>2 Methodologies</b>	<b>13</b>
2.1 Software and Basic Data Processing . . . . .	13
2.2 Multitaper Spectra . . . . .	13
2.3 Data Selection . . . . .	15
<b>3 Results and Discussion</b>	<b>17</b>
3.1 Replication of Previous Results . . . . .	17
3.2 Kermadec Events . . . . .	19
3.2.1 Seismogram Analysis . . . . .	19
3.2.2 Multi-station Analysis . . . . .	24
3.3 Discussion . . . . .	27
<b>4 Conclusions</b>	<b>31</b>
4.1 Future Work . . . . .	32
<b>References</b>	<b>33</b>



# List of Figures

1.1	Regional map of the Tonga-Kermadec subduction zone. Black dots are epicentre locations of earthquakes, all with magnitudes greater than $M_b5.0$ , analysed by van der Hilst and Snieder (1996) (MNG and SNZO mark the stations used for this analysis). The black dashed line denotes the location of the plate boundary at the surface, where the Pacific plate on the east is descending beneath the Australian Plate to the west. Figure from van der Hilst and Snieder (1996). . . .	8
1.2	A simple model of a homogeneous layer within two half-spaces. The half-spaces have a P-wave velocity of $c_0$ , while the layer has a different velocity of $c_1$ . The layer extends infinitely in the $x$ -direction. Figure after Fig. 19.11 of Snieder and van Wijk (2015). . . . .	10
2.1	Example Python script showing data download and calculation of the P-wave arrival. The event and station locations are plotted along with the waveform data.	14
2.2	Inventory of stations used in this study. All stations are broadband sensors, and only the vertical component was used. . . . .	15
2.3	Catalogue of earthquakes used in this study. The colour scale represents hypocentre depth, and the size of the marker gives the magnitude relative to the smallest magnitude of $M_W6.0$ . . . . .	16
3.1	Comparison of published and replicated filtered seismograms . . . . .	18
3.2	Location of the SNZO station and the epicentre positions of the earthquakes studied in Section 3.1 . . . . .	18
3.3	Comparison of published and replicated time-frequency plots . . . . .	19
3.4	Station locations and epicentre positions of the earthquakes studied in Section 3.2.1	20
3.5	Filtered seismograms of the events analysed in Section 3.2.1 . . . . .	21
3.6	Wigner-Ville spectrograms over the first 12 s of the earthquake arrivals for the seismograms shown in Figure 3.5 . . . . .	21
3.7	Comparison of spectrograms for increasing epicentral distance . . . . .	23
3.8	Frequency of occurrence of precursor observations by station . . . . .	24
3.9	Maps of earthquake epicentres classified by the observation of a precursor signal	25
3.10	Total number of precursory signals observed versus epicentre latitude . . . . .	26
3.11	Relationship between epicentre locations and the closest station at which a precursor was observed . . . . .	27
3.12	Depth slices of the New Zealand P-wave velocity model with station locations . .	30



# Chapter 1

## Introduction

Subduction interfaces produce some of the most dynamic, destructive, and complex geological and geophysical phenomena on the planet. Studying the processes and physical characteristics of subduction zones not only deepens our understanding of these environments, but also finds application in providing a framework for geological hazard assessment. The interaction of many geological, geophysical, and geochemical factors causes subduction zones to display heterogeneity over a wide range of scales, both within and between different interfaces. This study is concerned with the large-scale seismic heterogeneity within subducted oceanic lithosphere, which has been observed to cause anomalous dispersive propagation of seismic waves.

### 1.0.1 Dispersion in Subduction Zone Earthquakes

Several studies have revealed travel-time and frequency content anomalies in the seismograms of earthquakes at subduction zones around the Pacific (Abers, 2000). In central and northern Japan, high-frequency ( $f > 2$  Hz) and large intensity P-wave energy is observed from earthquakes originating at depth within the subducting Pacific plate (e.g. Iidaka & Mizoue, 1991; Furumura & Kennett, 2005). An initial low-frequency ( $f < 0.25$  Hz) arrival of energy at the time predicted by regional travel time tables is followed after 1-2 s by these high-frequency waves, which continue throughout a sustained long coda (Furumura & Kennett, 2005). Similar observations of low-frequency onsets followed by large intensity and high-frequency energy are reported for earthquakes at subduction zones in Alaska (Abers & Sarker, 1996), Taiwan (Chen et al., 2013), Vanuatu (Chiu et al., 1985), and South America (Martin et al., 2003). Common to all of these observations are the intermediate depths of the earthquake hypocentres (70-150 km) and the recording of the events at station arrays on the forearc side of the subducted plate.

The dispersive nature of these earthquakes is explained by the guiding of seismic energy up the subducted slabs. One model which explains this phenomenon consists of a relatively thin planar layer on the surface of the slab with a low seismic velocity compared to the surrounding mantle which acts to slow the propagation of short wavelength energy, while the longer wavelength energy passes unaffected (Abers, 2000; Martin et al., 2003). An alternative model invokes multiple internal scattering from anisotropic laminated structures within the plate to explain the efficient updip transmission of high-frequency energy to the surface, producing the large intensity anomalies (Furumura & Kennett, 2005). In either case, heterogeneity in the structure of the subducted plate is required to explain the anomalous dispersion. The characteristics of this heterogeneity affect the nature of the guided seismic energy recorded at the surface, including the magnitude of the velocity anomaly, and the thickness, mineralogy, continuity and extent of the low-velocity layer or anisotropic structures. Moreover, the hypocentre locations of earthquakes relative to the subducting slab, the locations of the receivers, and the source mechanisms and magnitudes of events are factors which have been shown to influence the nature of the anomalous dispersion observed at subduction zones (e.g. Martin et al., 2003; Love et al.,

2015; Chen et al., 2013; Gubbins et al., 1994).

Arrival time and frequency content anomalies are also observed for earthquakes originating within the Kermadec subduction zone (see Figure 1.1 for location). However, unlike the observations mentioned above, recordings of such earthquakes at seismometer stations in New Zealand display low amplitude high-frequency energy preceding the onset of low-frequency energy (Ansell & Gubbins, 1986; Gubbins & Snieder, 1991; van der Hilst & Snieder, 1996). These high-frequency precursors are observed to arrive a significant time before the predicted Jeffreys-Bullen P-wave arrival (sometimes  $>10$  s) after propagating up to 2000 km parallel to the strike of the subducting slab (Gubbins & Snieder, 1991). A model involving a continuous thin layer near the top of the subducting slab with a greater velocity than the surrounding mantle is proposed to explain the guiding of high-frequency energy at high velocity.

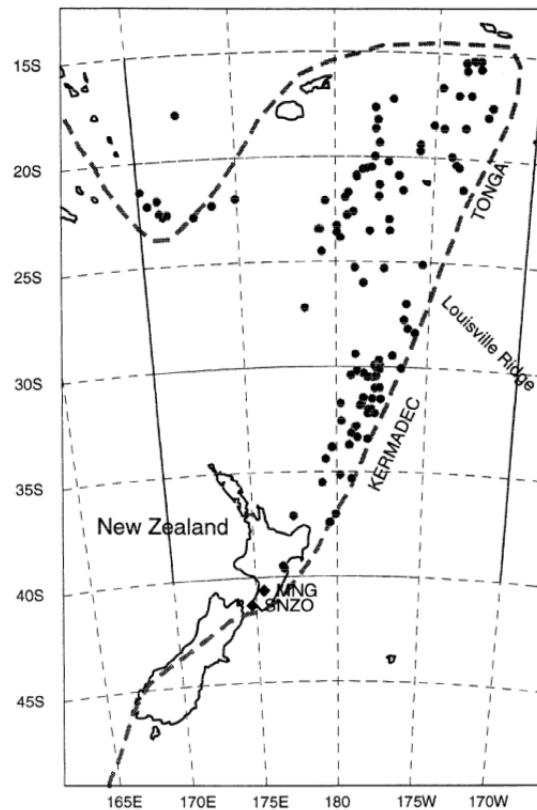


Figure 1.1: Regional map of the Tonga-Kermadec subduction zone. Black dots are epicentre locations of earthquakes, all with magnitudes greater than  $M_b 5.0$ , analysed by van der Hilst and Snieder (1996) (MNG and SNZO mark the stations used for this analysis). The black dashed line denotes the location of the plate boundary at the surface, where the Pacific plate on the east is descending beneath the Australian Plate to the west. Figure from van der Hilst and Snieder (1996).

This high velocity layer is interpreted to be composed of eclogite, a mineral resulting from the transformation of basaltic oceanic crust due to increasing temperatures and pressures as it descends into the mantle. In the Kermadec region, the high velocities are observed below a depth of 50 km, consistent with the conditions required to form eclogite. However, while some mineral compositions of eclogite have a velocity which is greater than the surrounding mantle, the relative velocity difference of approximately 2% is insufficient to explain the observed 5% dispersion using a single thin layer of eclogite (Gubbins & Snieder, 1991; Gubbins et al., 1994). As such, a more complex structure consisting of two layers with differing thicknesses and velocity anomalies within the slab has been proposed to explain the fast propagation of high frequencies over large distances (Gubbins & Snieder, 1991; van der Hilst & Snieder, 1996).

Love et al., 2015 report that the travel time and frequency content of waveforms from

earthquakes near the Hikurangi subduction zone beneath New Zealand are similar to those originating within the Kermadec subduction zone to the north. Low amplitude precursors containing energy at 4-9 Hz arriving at the times predicted by New Zealand tomographic velocity models are followed by a second phase of predominantly 2-4 Hz energy. A thin eclogite layer with a high seismic velocity over  $8.5 \text{ km s}^{-1}$  is invoked to explain these observations, consistent with tomographic models which reveal the presence of such high velocities at depths of 30-100 km beneath New Zealand (Eberhart-Phillips et al., 2010; Eberhart-Phillips & Reyners, 2012).

Previous studies of the high-frequency precursors recorded in New Zealand from earthquakes in the Kermadec region have used seismograms from analogue seismometers (Ansell & Gubbins, 1986) or from a limited number of digital seismometers at the southern end of the North Island (Gubbins & Snieder, 1991; Smith et al., 1994; van der Hilst & Snieder, 1996). Since that time, the New Zealand National Seismograph Network (NZNSN) has been greatly expanded and upgraded through the GeoNet project ([www.geonet.org.nz](http://www.geonet.org.nz)), creating a database with years of continuous digital waveform data from a dense broadband seismometer network covering New Zealand. In their study of the high-frequency precursors from earthquakes within New Zealand, Love et al. (2015) utilise the digital data from across the network to analyse the wave speed, frequency content, and polarization to gain information about the crustal and mantle structure. In this study, the digital waveform data from multiple GeoNet stations across New Zealand will be used to analyse the anomalous high-frequency precursors from earthquakes in the Kermadec subduction zone. The aim of this multiple-station analysis is to address several questions concerning the propagation of the precursors:

1. At what stations are high-frequency precursors observed?
2. How does the precursor change in frequency content, arrival time, and amplitude between stations?
3. What is the relationship between the hypocentre location and the stations at which high-frequency precursors are observed?

The answers which the results provide to these questions will be interpreted in light of the heterogeneity of the velocity structure within the subducted slab which is responsible for the anomalous dispersion.

### 1.0.2 Mathematical Description of Leaky Modes

The following explanation of guided waves establishes a theoretical basis for the anomalous dispersion of seismic waves propagating within subduction zones described in the previous section. This derivation follows the one given in Section 19.8 through 19.9 in Snieder & van Wijk, 2015, with further detail from Gubbins and Snieder (1991).

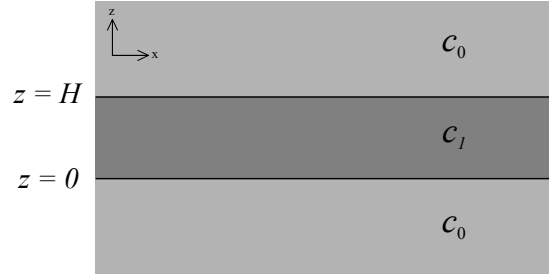


Figure 1.2: A simple model of a homogeneous layer within two half-spaces. The half-spaces have a P-wave velocity of  $c_0$ , while the layer has a different velocity of  $c_1$ . The layer extends infinitely in the  $x$ -direction. Figure after Fig. 19.11 of Snieder and van Wijk (2015).

For a simple model of the subsurface structure, we consider a homogeneous layer with a thickness  $H$  and P-wave velocity  $c_1$ , bounded above and below by two half-spaces with a P-wave velocity  $c_0$ , as shown in Figure 1.2. The velocity depends only on the  $z$  coordinate:  $c = c(z)$ . If  $u(x, z)$  represents the wave field in the frequency domain, then we may assume that the homogeneous Helmholtz equation is satisfied for a constant angular frequency  $\omega$ :

$$\nabla^2 u + \frac{\omega^2}{c(z)^2} u = 0 \quad (1.1)$$

In this model, the solution is invariant in the  $x$  coordinate, allowing us to express  $u(x, t)$  in terms of its Fourier transform:

$$u(x, z) = \int_{-\infty}^{\infty} U(k', z) e^{ik'x} dk' \quad (1.2)$$

Substituting this expression into equation (1.1) gives a homogeneous ordinary differential equation for  $U$ :

$$\frac{d^2 U}{dz^2} + \left[ \frac{\omega^2}{c(z)^2} - k'^2 \right] U = 0 \quad (1.3)$$

This equation has a solution of the form:

$$U(k', z) = A e^{-ikz} + B e^{+ikz} \quad (1.4)$$

where  $A$  and  $B$  are constants of integration and  $k = [\omega^2/c(z)^2 - k'^2]^{1/2}$ . Requiring that the waves outside the layer propagate away from the layer demands that  $A = 0$  for  $z > H$ , and  $B = 0$  for  $z < H$ . Also, the phase speed  $c(z)$  for a particular  $\omega$  is either  $c_0$  or  $c_1$ , allowing the solution to be written:

$$U(k', z) = \begin{cases} A e^{-ik_0 z} & z < 0 \\ C \cos k_1 z + D \sin k_1 z & 0 < z < H \\ B e^{+ik_0 z} & z > H \end{cases} \quad (1.5)$$

where  $k_0$  and  $k_1$  are given by:

$$k_0 = \sqrt{\frac{\omega^2}{c_0^2} - k'^2} \quad (1.6)$$

$$k_1 = \sqrt{\frac{\omega^2}{c_1^2} - k'^2} \quad (1.7)$$

Imposing the condition that  $U$  and  $dU/dz$  are continuous at the layer boundaries yields a linear system of four equations containing the four unknowns  $A$ ,  $B$ ,  $C$ , and  $D$  (Snieder & van Wijk, 2015). Solving this system requires that the following dispersion relation holds for these guided waves:

$$\tan(k_1 H) = -\frac{2ik_0 k_1}{k_1^2 + k_0^2} \quad (1.8)$$

This equation constrains the values which  $k'$  can have, as  $k_0$  and  $k_1$  are both functions of  $k'$  for a given  $\omega$ . Thus, we see that this system only allows waves to propagate when equation (1.8) holds; these waves are called guided waves.

An important result of this analysis is the dependence of  $k'$  on  $\omega$  (i.e  $k' = k'(\omega)$ ). This implies that the phase velocity of a guided wave is dependent on the frequency:  $c(\omega) = \omega/k'(\omega)$ . Hence, the guided waves are dispersive waves, since different frequencies propagate at varying speeds. The nature of this dispersion is determined by the relationship between the seismic velocity  $c_1$  of the layer and the seismic velocity  $c_0$  of the half-spaces. Of interest here is the propagation of seismic waves within a high velocity layer.

A high velocity layer is one for which  $c_1$  is greater than  $c_0$  in Figure 1.2. This implies  $\omega/c_1 < \omega/c_0$ . For a wave source of finite energy, we must impose the condition that the amplitude within the upper and lower half-spaces decreases with distance away from the layer (Gubbins & Snieder, 1991). Examining the solution (1.5) and expressions (1.6) and (1.7), we see that this condition is satisfied if  $\omega/c_1 < k' < \omega/c_0$ , with the solution being:

$$U(k', z) = \begin{cases} Ae^{k_0 z} & z < 0 \\ C \cos [i\kappa_1 z] + D \sin [i\kappa_1 z] & 0 < z < H \\ Be^{-k_0 z} & z > H \end{cases} \quad (1.9)$$

where  $\kappa_1$  is the coefficient of the imaginary part of  $k_0$ , which is purely imaginary. This causes the dispersion relation to become:

$$i \tanh(\kappa_1 H) = -\frac{2k_0 \kappa_1}{\kappa_1^2 - k_0^2} \quad (1.10)$$

This implies that the expression  $2k_0 \kappa_1 / (\kappa_1^2 - k_0^2)$  must be imaginary in order for (1.10) to hold, which is satisfied only for complex values of  $k'$ . Since the waves in this model are described by the function  $U(k', z)e^{i(k'x - \omega t)}$ , a complex wavenumber implies that:

$$U(k', z)e^{-\text{Im}(k')x} e^{i[\text{Re}(k')x - \omega t]} \quad (1.11)$$

Hence, a high velocity layer gives rise to guided waves which must exponentially decay in amplitude as they propagate in the  $x$ -direction, due to the  $e^{-\text{Im}(k')x}$  term. Further analysis reveals that the exponential decay is caused by energy propagating away from the high velocity layer. This is due to waves refracting, or “leaking”, away from the high velocity material according to Snell’s Law, leading to these guided wave being referred to as leaky modes (Snieder & van Wijk, 2015).

An approximation of group velocity as a function of frequency for these leaky modes in this model is derived in Gubbins and Snieder (1991). Its expression is:

$$c_g = c_1 \left( 1 - \frac{n^2 \pi^2 c_1^2}{2\omega^2 H^2} \right) \quad (1.12)$$

where  $n$  is an integer representing the overtone number of the leaky mode. This equation clearly shows that the group velocity of the leaky modes propagating within the high velocity layer is inversely related to the frequency—the higher frequencies travel faster than the slower frequencies. Moreover, the expression of the wavelength for the  $n^{\text{th}}$  overtone is  $\lambda_n = 2H/n$ , showing that the wavelength (and frequency) of the leaky modes depends on the thickness of the high velocity layer (Gubbins & Snieder, 1991).

## Chapter 2

# Methodologies

### 2.1 Software and Basic Data Processing

All data processing and analysis for this study was performed using the programming language Python, with extensive use of ObsPy, an open-source seismology library for Python. ObsPy provided a versatile collection of functions to implement all aspects of the seismological data analysis, from reading and writing data files, retrieving waveform data and event information, and filtering and plotting traces (Beyreuther et al., 2010; Krischer et al., 2015). Also, routines from the extensive libraries which Python provides for scientific analysis, including matplotlib for data display (Hunter, 2007) or NumPy for array manipulation (see <http://www.numpy.org>), were easily incorporated into the code. Using this approach allowed a large degree of flexibility in the analysis and display of the data.

Searches were made of the GeoNet FDSN (The International Federation of Digital Seismograph Networks) webservice for earthquakes and stations relevant to this study. After retrieving a suitable catalogue of events, the waveform data was downloaded at each station for a length of 500 seconds from the origin time of each earthquake. Since the earthquakes occurred in the Kermadec region, the arrival of the signal at New Zealand stations was captured in full by this time interval. An inventory of stations was also compiled which included the instrument responses. Since the seismogram recorded on a seismometer is the convolution of the ground motion at the site with the frequency response of the instrument and any digital amplifiers or filters, the seismograms must be corrected by deconvolving with the instrument response to retrieve the true ground motion (Krischer et al., 2015). This instrument correction was applied before processing the waveforms further.

For each event studied, the arrival time of the first P-wave (i.e. the P phase) was estimated in order to provide a standard of comparison for precursory energy. The iasp91 symmetric Earth velocity model was used with the ObsPy `taup` library to calculate these arrival times (Kennett & Engdahl, 1991; Krischer et al., 2015). For all time-series plots of the traces,  $t = 0$  is taken to be the time of the predicted P-wave arrival, rather than the origin time of the earthquake, as the former provides a convenient means of comparison between the waveforms of different events when multiple stations are considered. Figure 2.1 shows an example Python script which downloads an event catalogue, a station inventory, and waveform data, and then calculates the predicted P-wave arrival and plots the results.

### 2.2 Multitaper Spectra

In order to analyse the frequency content of seismograms to identify and characterise the leaky mode and frequency dispersion, a robust technique must be employed to accurately represent the signals in the frequency domain. This corresponds to estimating the power spectral density (PSD) function of the signal  $x(t)$ , which is found by computing:

```

1 from obspy.clients.fdsn import Client
2 from obspy import UTCDateTime
3 from obspy.taup import TauPyModel
4 from obspy.geodetics import locations2degrees
5
6 client = Client('http://beta-service.geonet.org.nz')
7
8 #Download a catalogue of events
9 events = client.get_events(minlatitude=-37,maxlatitude=-25,\
10                          minlongitude=-180,maxlongitude=-175,minmagnitude=6.0,\
11                          starttime=UTCDateTime("2014-01-01T00:00:00"),\
12                          endtime=UTCDateTime("2014-06-28T23:58:59"))
13
14 #Retrieve the station information for MWZ
15 inventory = client.get_stations(network="NZ",level="response",station="MWZ")
16
17 #Get the waveform data for the first event at station MWZ
18 origin_time = events[0].origins[0].time
19 stream = client.get_waveforms("NZ", "MWZ", "*", "HHZ",origin_time,origin_time+500)
20
21 #Calculate the predicted arrival time of the P phase
22 model = TauPyModel(model="iasp91")
23 event_lon = events[0].origins[0].longitude
24 event_lat = events[0].origins[0].latitude
25 event_depth = events[0].origins[0].depth/1000
26 epicentral_dist = locations2degrees(event_lat, event_lon,\
27                                   inventory[0][0].latitude, inventory[0][0].longitude)
28 arrival_P = model.get_travel_times(distance_in_degree=epicentral_dist,\
29                                   source_depth_in_km=event_depth,phase_list=['P'])
30
31 #Plot the event locations, the station, and the trace of the first event
32 events.plot(), inventory.plot(), stream.plot()

```

Figure 2.1: Example Python script showing data download and calculation of the P-wave arrival. The event and station locations are plotted along with the waveform data.

$$\hat{S}(f) = \left| \sum_{t=0}^{N-1} x(t)a(t)e^{-2\pi ift} \right|^2 \quad (2.1)$$

where  $N$  is the number of samples in the discrete time series  $x(t)$ ,  $f$  is the frequency, and  $a(t)$  is a weighting function called a taper (Prieto et al., 2007). One purpose of the taper is to calculate the PSD function of a signal for a select interval of time by letting  $a(t) = 0$  outside the interval. More importantly, the taper serves to reduce spectral leakage—the transfer of power from one frequency of the PSD to another due to the nature of the mathematical operation performed in Equation (2.1). To achieve this purpose, all effective tapers will cause the signal to smoothly reduce or tend to zero at the beginning and end of the time interval (Percival & Walden, 1993).

Since the taper must reduce the amplitude at the upper and lower limits of the time series  $x(t)$ , a significant portion of the signal is lost. In order to reduce spectral leakage while retaining as much information from the signal as possible, multitaper techniques are used. Instead of using a single taper, the power spectral density function is calculated multiple times with several orthogonal functions as the tapers, and the total spectral estimate is obtained by adding these single-taper PSD functions in a weighted sum. The multitaper functions are chosen such that the spectral leakage and the amount of signal discarded are both minimised (Prieto et al., 2007).

Along with providing a robust technique to estimate the spectral composition of a seismogram, multitaper processes can also be applied to frequency versus time spectrograms. Prieto et al. (2005) demonstrated that using a multitaper with a Wigner-Ville spectrum in order to compute a spectrogram reduced smearing of frequencies, increasing the resolution between fundamental frequencies and overtones. This allowed for a more detailed analysis of dispersion in the context of surface wave tomography. One disadvantage of the Wigner-Ville multitaper spectrogram is the presence of interference terms between the fundamental frequencies and unrelated distant frequencies. This can reduce the prominence of the fundamental frequencies, but the effect can be lessened by applying a Gaussian filter during the computation with compromise of a slight reduction in the resolution of the spectrogram along the time axis.

These multitaper techniques were applied to the seismograms of candidate earthquakes using the Python wrapper for the multitaper library described in Prieto et al. (2009). The primary parameter to be defined when using the Python functions is the time bandwidth product, which is the averaging bandwidth for which the multitaper spectra are calculated. Increasing this parameter causes spectral peaks to be smoothed in the frequency domain; unless otherwise stated, a time bandwidth product of 3.5 was determined to produce a satisfactory balance between resolution and smoothing. Moreover, spectrograms are displayed using a colour scale of decibels above the median value in order to enhance the contrast of distinctive features.

## 2.3 Data Selection

The GeoNet earthquake event catalogue was searched to find candidate events from the Kermadec region which may contain precursory high-frequency arrivals. The operational periods of GeoNet seismometers and results from previous studies of Kermadec events were used to constrain the parameters of the search.

van der Hilst and Snieder (1996) report that for earthquakes occurring along the subducting Pacific Plate to the north of New Zealand, early arrivals of high-frequency energy is only observed for earthquakes in the latitude range of 25°S to 37°S. As such, the search for events displaying a high-frequency precursor was contained to 25°S to 37°S of latitude and 175°E to 170°W of longitude. No constraint was placed on the depth of the events due to the large range of depths for which dispersive phenomena is reported (van der Hilst & Snieder, 1996; Gubbins & Snieder, 1991), and the minimum magnitude of the earthquakes was set at  $M_W 6.0$ . This magnitude constraint was imposed to provide an adequate signal-to-noise ratio at stations in New Zealand and to limit the total amount of data to be analysed at multiple stations.

An inventory of GeoNet seismometers for which data was to be downloaded was determined on the basis of geographical location. Stations were selected along the east coast of the North and South Islands so that energy propagating within and parallel to the subducted slab could be analysed as it travelled down the country. The time range over which the search was performed was then chosen to align with the period of operation of the seismometers. Figure 2.2 shows the stations for which waveform data was downloaded for candidate earthquakes occurring between 1<sup>st</sup> March 2004 (UTC) and 31<sup>st</sup> December 2016 (UTC), a period of 11 years and 10 months. Figure 2.3 shows the earthquakes in this time period which satisfied the event criteria.

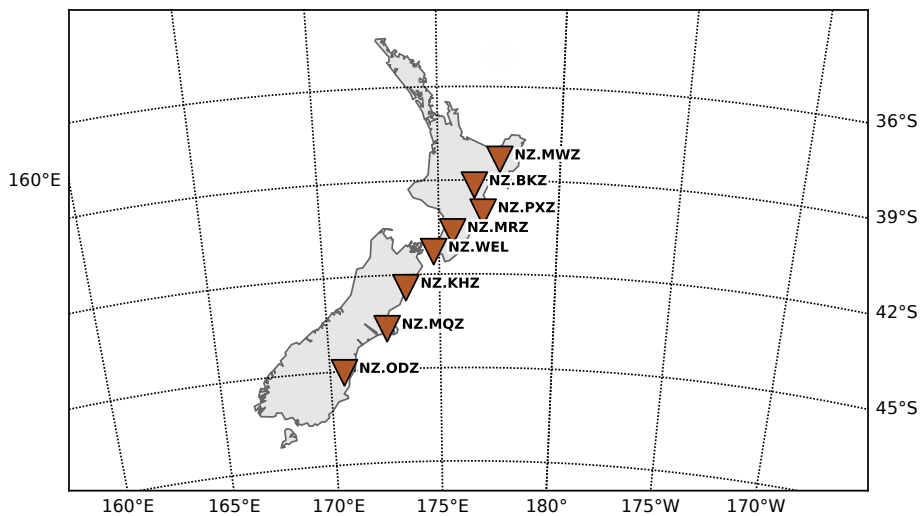


Figure 2.2: Inventory of stations used in this study. All stations are broadband sensors, and only the vertical component was used.

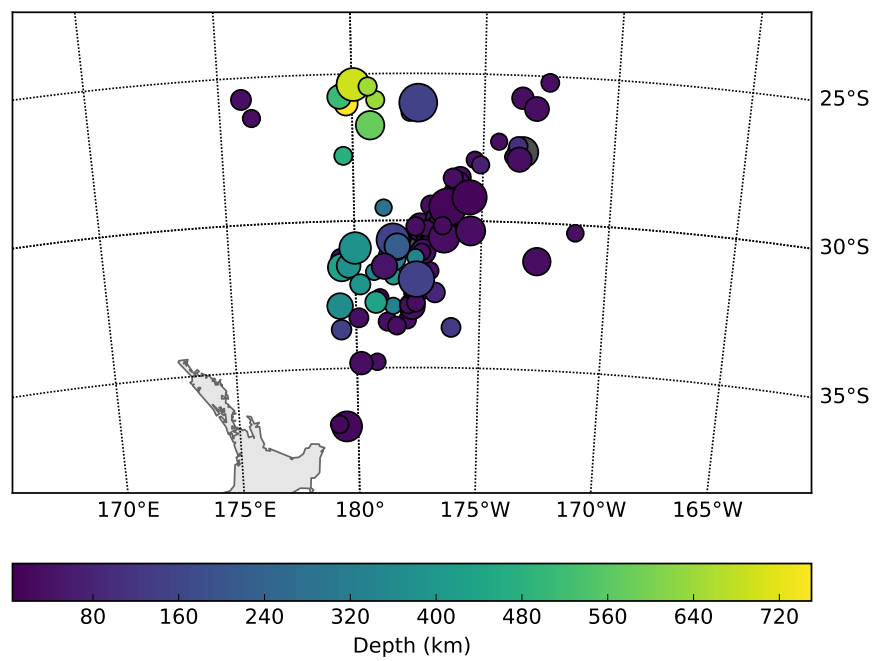


Figure 2.3: Catalogue of earthquakes used in this study. The colour scale represents hypocentre depth, and the size of the marker gives the magnitude relative to the smallest magnitude of  $M_W 6.0$ .

## Chapter 3

# Results and Discussion

### 3.1 Replication of Previous Results

In order to verify the methods which were used to study the leaky modes, previous results from the literature were first replicated. Successfully reproducing past results served to provide confidence that the analysis tools used in this study were suitable for analysing a larger number of earthquakes recorded at many more stations than in the past.

Plots of filtered seismogram traces recorded on the short period vertical component of the SNZO station at Wellington are used to demonstrate the dispersion of seismic energy from earthquakes originating in the Kermadec subduction zone in both Gubbins and Snieder (1991) and van der Hilst and Snieder (1996). These plots function as an appropriate standard of comparison, as the technique of filtering the seismic data is fundamental to understanding the dispersion present in the seismograms. Moreover, the waveform data is readily available from the Incorporated Research Institutions for Seismology (IRIS) database.

Figure 3.1 shows filtered seismograms of an earthquake originating in the Kermadec subduction zone which has a high-frequency onset at SNZO near Wellington (see Figure 3.2 for the location). The lowpass and highpass filters separate the higher frequencies from the lower frequencies, demonstrating that the initial emergent onset of the earthquake contains only frequencies above 2 Hz which arrive over 10 s before the predicted P phase. Filtering the traces also aids in the identification of both the first arrival of the high frequency energy and also the later arrival of the lower frequency energy. The filters employed by Gubbins and Snieder (1991) for this figure are one lowpass and two highpass causal filters with corner frequencies of 1 Hz, 2 Hz, and 5 Hz, respectively, which preserve the original onset time of the signal.

A comparison of the waveforms between the original figure and the replica suggests that the unfiltered trace of the original figure does not contain the long wavelengths with periods on the order of 5 s seen in the unfiltered trace of the replica, nor are the very high frequencies in the 5 Hz highpass filter of the replica present in the same filtered trace of the original figure. One possible reason for the apparent difference in the upper and lower limits of the frequency content of the data may be the pre-filter applied before the seismometer response is removed. Although Gubbins and Snieder (1991) do not mention whether a pre-filter has been applied to the data, the pre-filter used for the seismograms in this study was constructed with conservative corner frequencies at 0.1 Hz and 50 Hz. This would allow both the long and short wavelengths not observed in the original trace to be present in the data used for the replica.

Apart from the presence of higher frequencies than in the original figure, the waveforms of the highpass filters between the two figures are very similar. However, the arrival time pick of the high frequency energy for the replica has been placed over three seconds after the time indicated in the original figure, and the initial arrival of low frequency energy can not be defined in the replica as in the original. The reason for the difficulty in reproducing the exact arrivals is again due to the apparent difference between the lowest and highest frequency ranges, as

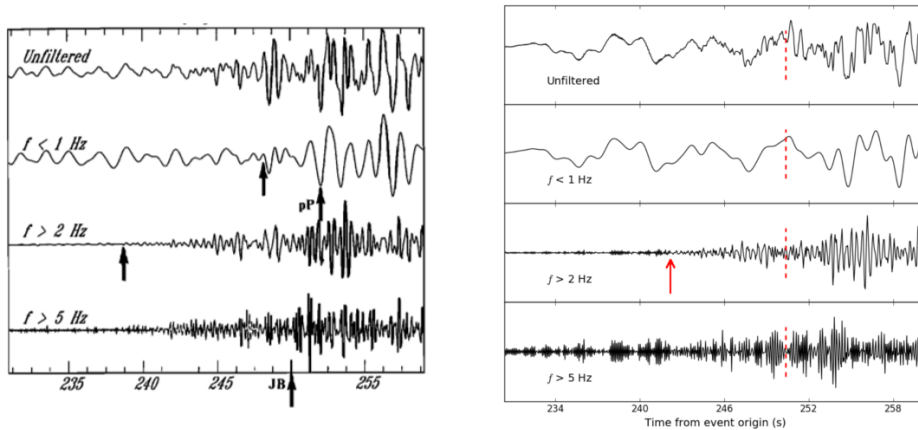


Figure 3.1: Comparison of published and replicated filtered seismograms. The left panel is Figure 2 from Gubbins and Snieder (1991) and the right panel is a replica using data from the same event. First break picks of the filtered signal are indicated by the unlabelled arrows in the respective filtered traces. The arrow marked JB (for Jeffreys-Bullen times) and the red dashed line indicate the predicted arrival times of the P phase. See Figure 3.2 for the location of the  $M_b$ 5.9 event.

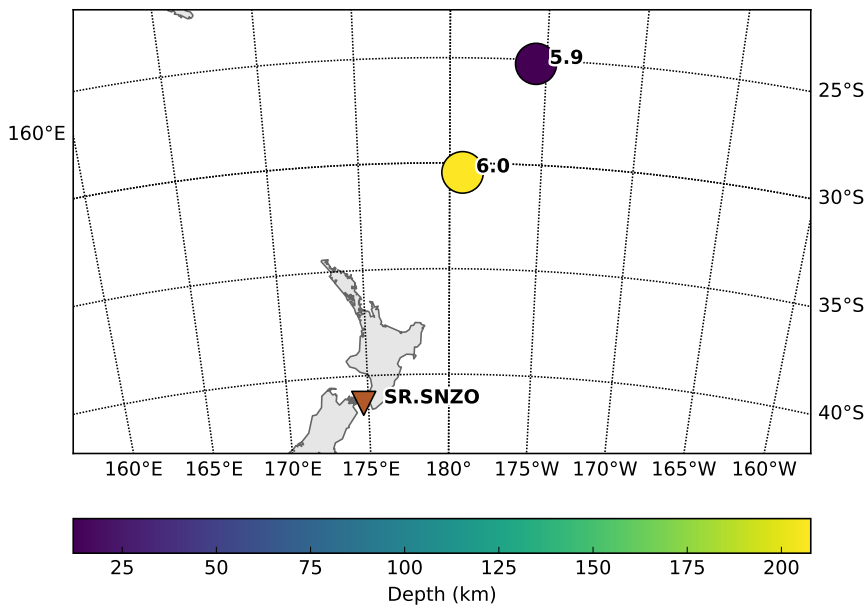


Figure 3.2: Location of the SNZO station and the epicentre positions of the earthquakes studied in Section 3.1.

the first breaks of the signal in each frequency band are masked by high or low frequencies not present in the original figure. However, the replica clearly separates the high frequency precursory energy from the lower frequency signal as in the original figure, and although the first arrivals have not been picked at the same locations, this replication of results verifies the use of the multiple filtering technique for identifying the leaky mode signal in seismograms.

Another method to analyse the dispersion of the seismograms involves plotting the traces in the time-frequency domain. Time-frequency plots are generated by Gubbins and Snieder (1991) by applying a series of acausal zero-phase Gaussian bandpass filters to a seismogram with varying centre frequencies. The resulting amplitude contours, which are equalised in each frequency band, are then displayed in plots of frequency against time. This technique was reproduced

by bandpass filtering the seismogram with overlapping frequency windows centred at different values. The Wigner-Ville spectrogram was then computed for each of the resulting traces, and the individual spectrograms were combined to form a single time-frequency representation of the trace.

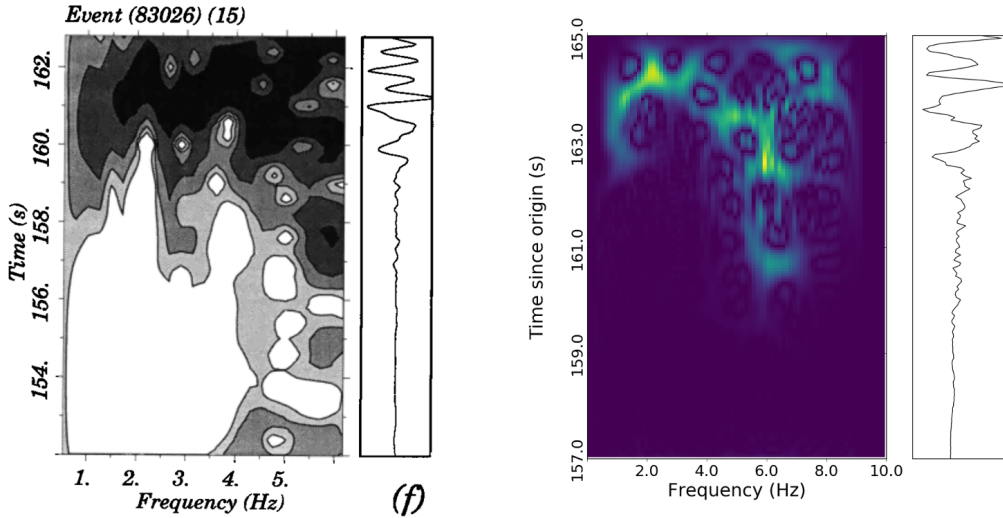


Figure 3.3: Comparison of published and replicated time-frequency plots. The left panel shows Figure 5(f) from Gubbins and Snieder (1991) and the right panel is a replica using the same data. The  $M_b$ 6.0 earthquake has a hypocenter at 238 km depth, as shown in Figure 3.2.

Figure 3.3 shows a spectrogram computed in this way, along with the corresponding original time-frequency plot (Figure 5(f) from Gubbins and Snieder (1991); see Figure 3.2 for the location of this event). Frequency windows of 2 Hz width centred at 1 Hz intervals from 1-9 Hz were used for consecutive bandpass filters. A difference of 4 s in the initial arrival of the energy between these two plots is due to a time offset in the downloaded data. High frequency energy at 6 Hz is recorded for 3 s before lower frequency energy arrives, clearly visible in both of the plots. In fact, the resolution of this high frequency signal in the frequency domain of the replica appears greater than in the original plot. This greater resolution may be due to the reduction in spectral leakage owing to the multitaper Wigner-Ville filter, or it may be a result of the particular window size of the bandpass filter. Regardless, the methods used to create the replica appear to have reduced the smearing from the Gaussian filters, and the nonzero values in the original plot caused by noise or filtering artefacts are absent in the replica.

The details of the parameters used to plot the Wigner-Ville spectrograms in the study is given in Appendix A.

## 3.2 Kermadec Events

### 3.2.1 Seismogram Analysis

An initial search for high-frequency leaky modes in the seismograms was performed by analysing the arrival of seismic energy at the station MWZ near the East Cape of the North Island (see Figure 3.4 for the location of this station). Leaky modes were identified as a low amplitude, higher frequency signal superposed on lower frequency noise, arriving before the initial onset of P-wave energy. The station MWZ was chosen for this initial analysis, as it is one of the first GeoNet seismometers to record earthquakes propagating parallel to the strike of the slab. Thus, the effect of energy loss in the leaky mode due to refraction from the high-velocity layer is less significant than other stations further south. Moreover, only low levels of long-term noise were observed at this station, increasing the signal-to-noise ratio in the seismograms.

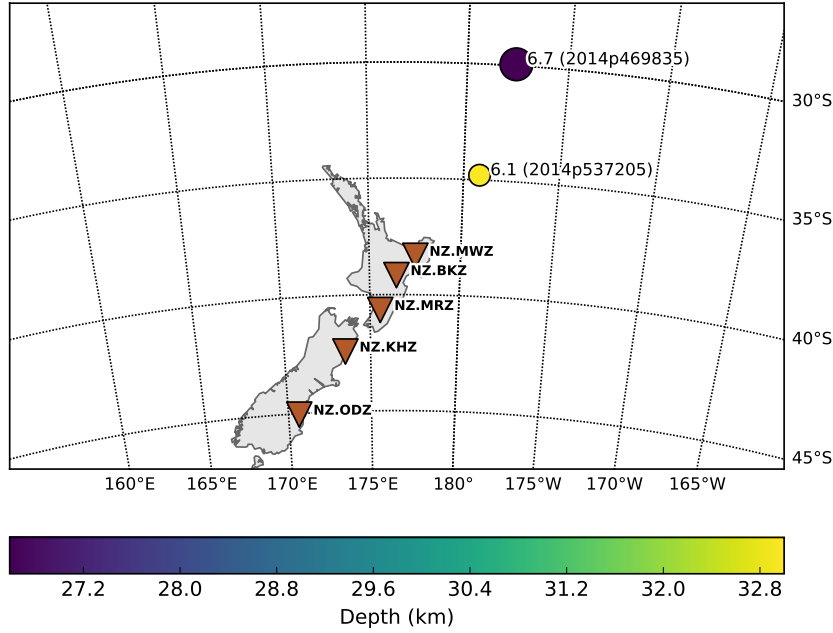


Figure 3.4: Station locations and epicentre positions of the earthquakes studied in Section 3.2.1. The depth of the earthquakes are shown by the colour scale, and the  $M_W$  magnitude of each event is stated next to the circle with the GeoNet catalogue ID given in brackets.

Figure 3.5 shows the seismograms of two earthquakes with hypocentres near the subducting Pacific plate interface, recorded at MWZ. The earthquakes share similar magnitudes and hypocentre depths, but the larger  $M_W$ 6.7 earthquake is approximately twice as far from MWZ as the smaller  $M_W$ 6.1 event (see Figure 3.4). The left panel of Figure 3.5 shows that the larger event contains high frequency precursory signal. The highpass and lowpass filters reveal that this high frequency energy above 2 Hz has an emergent onset, arriving at MWZ approximately 5 s before the predicted P-wave arrival and 8 s before the onset of lower frequency energy below 1 Hz. In contrast, the right panel of Figure 3.5 shows the smaller event does not have a high frequency precursory arrival; the energy in each frequency band arrives at the same time. However, at this stage in the analysis, we cannot exclude the possibility that some of the energy followed ray paths through the high velocity layer. Figure 3.5 also shows that the amplitude of the high frequency energy which arrives before the predicted P arrival is an order of magnitude less than the amplitude of both the low and high frequency energy arriving after 4 s. A low amplitude high frequency signal is observed between 0 s and 2 s in the second event, but unlike in the first event, this low amplitude signal occurs at the same time as the low frequency signal and is four times shorter in duration.

In order to analyse the frequency content more carefully, the spectrograms of these seismograms were computed for the first 12 s of the earthquake arrival. The high frequency onset of the larger event contains distinct narrow width bands of three different frequencies centred at 3 Hz, 5 Hz, and 7 Hz (left panel of Figure 3.6). The earliest of these peaks at 7 Hz appears as a 1 s burst on the spectrogram, while the 5 Hz band continues through remainder of the time period shown, increasing in intensity over time. The band of 3 Hz energy arriving 4 s before the predicted P-wave arrival also continues through the entire time interval, but dispersion toward lower frequencies after -2 s occurs at a rate of approximately 0.5 Hz per second. No such dispersion is visible in the spectrogram of the smaller event (right panel of Figure 3.6), as there is very little separation between the arrival times of frequencies from 1-6 Hz. The spectrogram is dominated by a band of energy centred at 2 Hz, with peaks of lower intensity at a 4 Hz and 6 Hz.

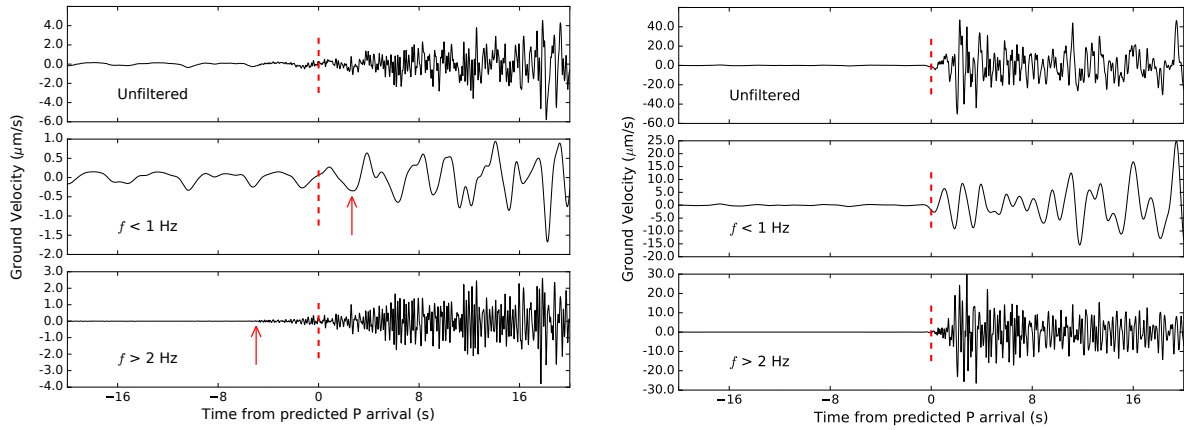


Figure 3.5: Filtered seismograms of the events 2014p469835 (left) and 2014p537205 (right) recorded at MWZ. Figure 3.4 gives the hypocentre and magnitude information. The approximate arrivals of the signals are indicated by the red arrows in the different frequency bands. A highpass filter at 0.2 Hz was applied to remove large amplitude long period features.

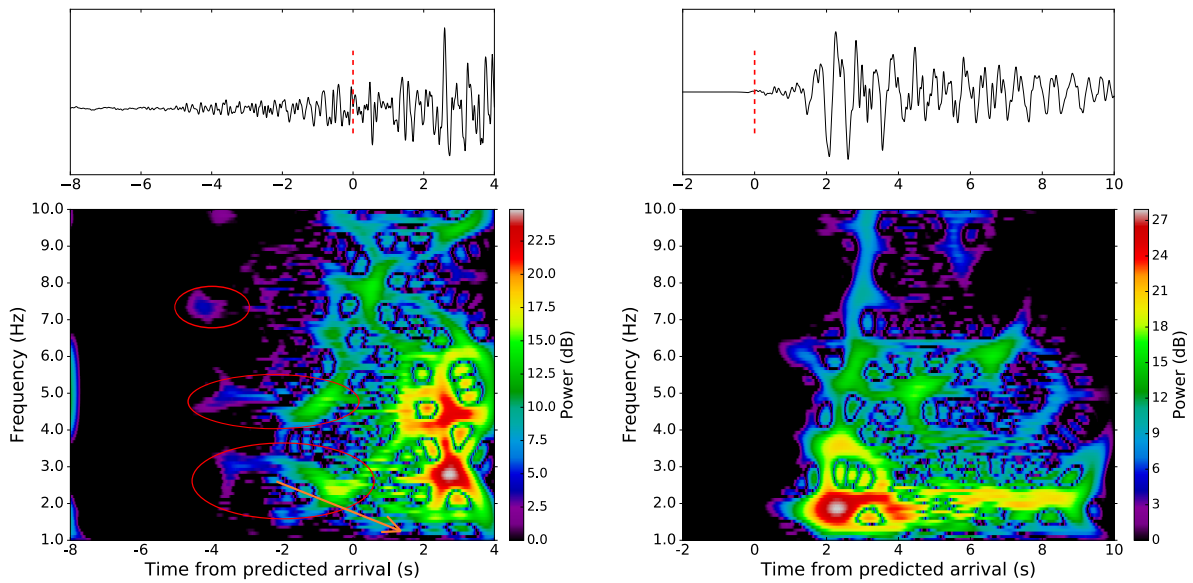


Figure 3.6: Wigner-Ville spectrograms over the first 12 s of the earthquake arrivals for the seismograms shown in Figure 3.5. The frequency content of emergent precursor for event 2014p469835 (left) is characterised in the spectrogram by three distinct peaks, as outlined in red. The orange arrow shows a decrease in the frequency content of the seismogram with time.

Having analysed the arrival of these earthquakes at MWZ in both time and frequency, the question naturally arises concerning the cause of the obvious differences between arrival time, frequency content, and relative amplitude. For earthquakes recorded at the same station with little background noise, the variables which influence the characteristics of the waveform are the magnitude, the hypocentre location relative to the high velocity layer and the station (which determines the ray paths), and the focal mechanism. Previous studies of precursory arrivals from the Kermadec region rule out the depth and the magnitude (above a certain minimum signal-to-noise threshold) as influencing factors for whether or not a precursor is observed. However, the epicentre location and the focal mechanism are shown to be influencing factors (Gubbins & Snieder, 1991; van der Hilst & Snieder, 1996; Love et al., 2015). The orientation of the nodal planes of the moment tensors for these earthquakes are significantly different (USGS REFERENCE), so this may be one reason for the absence of a precursor in the seismogram

of the smaller event. The effect of the distance between the epicentre and the station may be tested by analysing the arrivals of these earthquakes as the energy propagates southward down New Zealand.

Figure 3.7 shows a comparison between the spectrograms of the initial arrival of energy for the two events at seismometer stations along the East Coast of New Zealand. The station-epicentre distance increases from top to bottom, as shown by the station locations in Figure 3.4. The amount of time by which the first arrival of the signal precedes the predicted P-wave arrival increases with epicentral distance, especially for the second event where the negative first break residual increases from 0 s at MWZ to -6 s at ODZ. High-frequency energy above 3 Hz arrives before lower frequency energy for the first event in a similar manner to that observed in Figure 3.6 at the three North Island stations (MWZ, BKZ, MRZ). Also, it appears that the previously observed frequency bands centred at 3 Hz and 5 Hz at MWZ for the first event increase in frequency to 4 Hz and 6 Hz at BKZ and MRZ, while the 7-8 Hz peak increases to 8-9 Hz at these stations. Once the signal propagates to the South Island (KHZ and ODZ), the clear precursory high frequency energy peaks of the first event are no longer clearly visible, and the lower frequency energy arrives first.

On the other hand, the frequency content of the first arrival for the second event increases with station-epicentre separation in Figure 3.7. High frequency energy above 3 Hz arrives at the same time as or later than the lower frequency energy at MWZ and BKZ, but at MRZ, a peak centred at 4 Hz dominates the first arrival, with a smaller peak at 7 Hz. Also, clear dispersion of the dominant frequency content from 4 Hz to 1 Hz occurs over the first 6 s of the earthquake at MRZ. At KHZ, the frequency separation is not so pronounced, although the first arrival is peaked at 5 Hz. However, the dispersion at ODZ is very obvious over the first 2 s of the arrival where the signal decreases from 8 Hz to 2 Hz. The spectrograms of the second event demonstrate that a high frequency dispersive arrival develops as the distance over which the energy propagates increases, demonstrating that the station-epicentre distance is an influencing factor for whether a precursor is observed for this particular event.

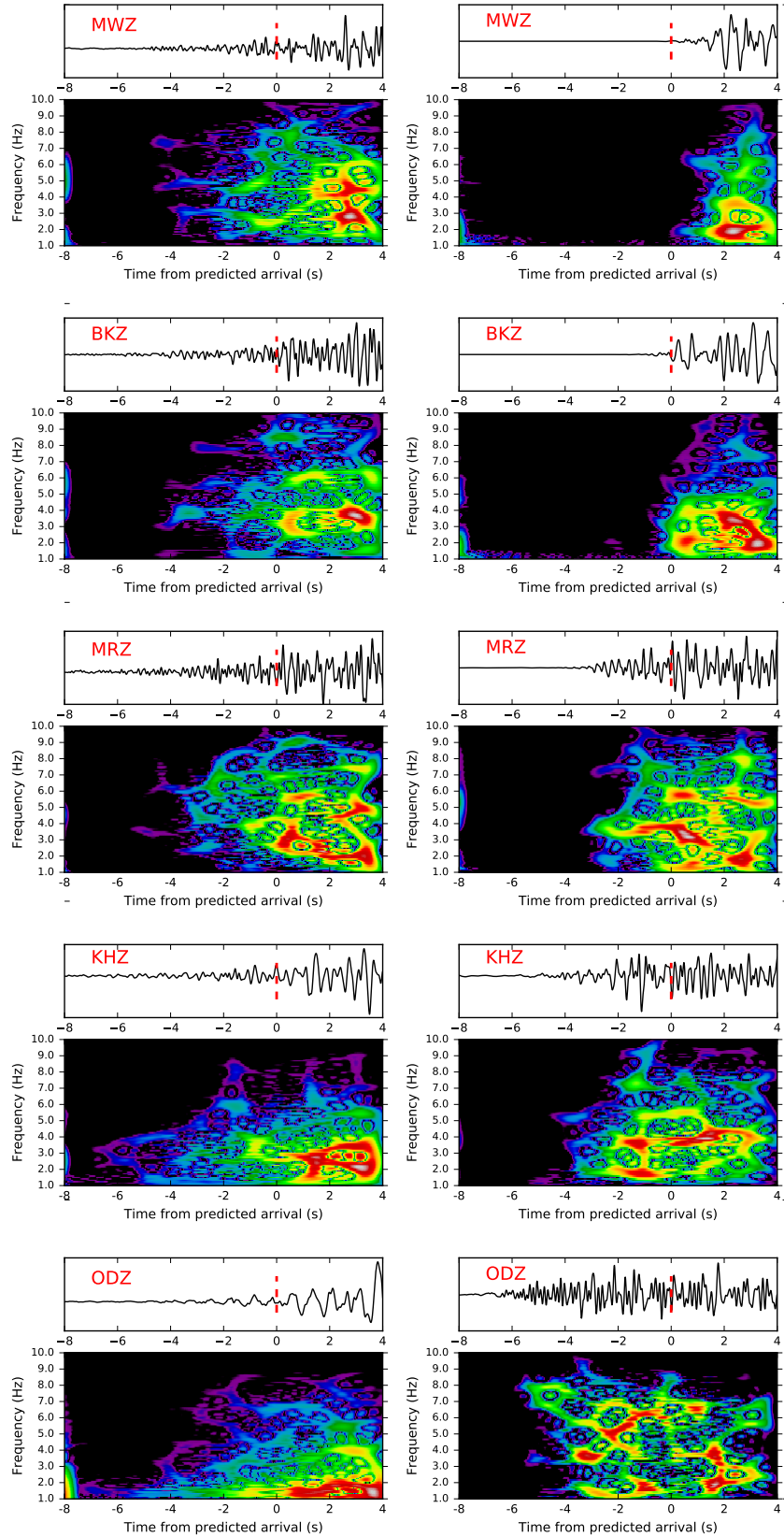


Figure 3.7: Comparison of spectrograms for increasing epicentral distance. The left column shows spectrograms for event 2014p469835, and the right column shows spectrograms for event 2014p537205. Station-epicentre distance increases from top to bottom (see Figure 3.4 for station locations).

### 3.2.2 Multi-station Analysis

Having established that the distance between an earthquake epicentre and a seismometer station influenced the detection of a high frequency precursor for the two events studied in Section 3.2.1, an analysis of the entire dataset was performed in order to explore this relationship further. This analysis was carried out by generating spectrograms for all 97 events in the catalogue at all eight stations in the inventory. Wigner-Ville spectrograms with the same filtering constraints as in Figure 3.7 were computed at each of these stations for a time interval spanning -15 s to 5 s about the predicted P-wave arrival, capturing the first arrival of energy at each station.

The results of Section 3.2.1 determined the criteria for identifying the high frequency precursors in the spectrograms. Figure 3.7 showed that peaks of energy above 3 Hz arrive before signal of lower frequencies at stations where high-to-low frequency dispersion is observed. Thus, a seismogram was marked as containing a high frequency precursor where energy above 3 Hz arrived at least 1 s before energy below 3 Hz. The 1 s threshold is considered a realistic minimum value for distinguishing a precursor in time from signal of lower frequency or noise in the spectrograms. A record was also made of the seismograms for which no such precursor was observed or where large amplitude background noise masked the arrival of signal. Table A.1 shows the results of this analysis for all events and stations.

For the events analysed, a precursor was observed in the spectrogram of at least one station for 53 events, while no precursor was observed at any station for 44 events. Of the events where no precursor was observed, the arrival was not visible due to poor data quality at all stations for four events. Only three of the events analysed showed a precursor at all stations. The distribution of the number of precursors observed at each station is shown in Figure 3.8. MRZ was the station for which the most precursors were observed (48), while the southernmost station ODZ showed the least amount of precursors (10). Background noise which prevented an arrival pick at the Wellington station (WEL) occurred almost twice as often as at other stations, but WEL was included due to its potentially significant geographical location at the bottom of the North Island.

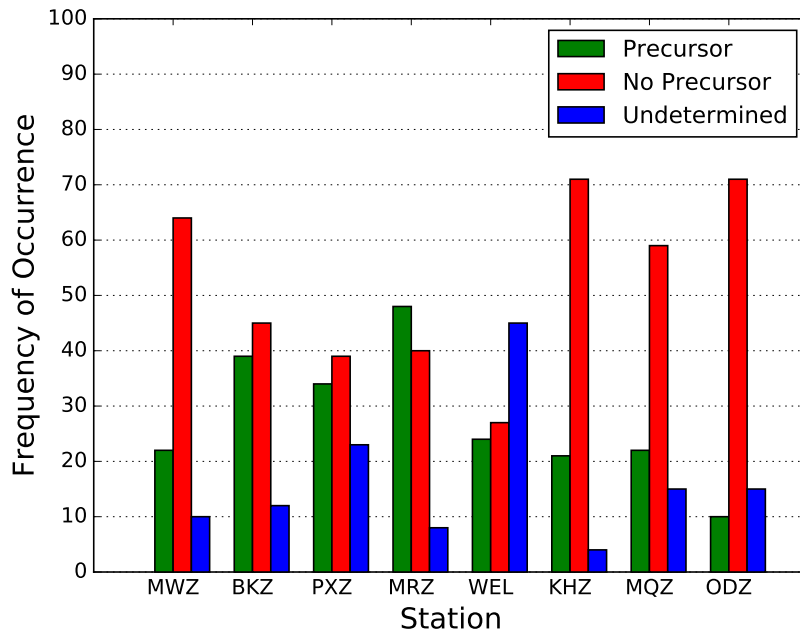


Figure 3.8: Frequency of occurrence of precursor observations by station. "Undetermined" indicates that large amplitude background noise prevented a decision being made on the presence of a precursor.

Maps of the earthquake epicentres were plotted for events where no precursor was observed at any station and for events where a precursor was observed at one or more stations (see Figure 3.9;

note that the first map also contains events for which noise masked the first arrival). These maps clearly show that the earthquakes which generated an observable precursor are grouped in a geographical region extending from 25°S to 35°S parallel to the strike of the subducted slab. The spread of the epicentres for which no precursor is observed is greater, showing that earthquakes to the east of the subduction zone as well as those deep within the backarc region to the west do not produce observable precursors. Precursory arrivals are observed from earthquakes with hypocentres over a large depth range, and it appears that the depths increase from east to west. This suggests that the earthquakes generating leaky modes occur in close proximity to the descending slab. Notice also that the magnitude of the earthquakes (above  $M_W 6.0$ ) does not appear to be a factor influencing the observation of precursors, consistent with the conclusions of previous studies (Gubbins & Snieder, 1991; van der Hilst & Snieder, 1996; Love et al., 2015).

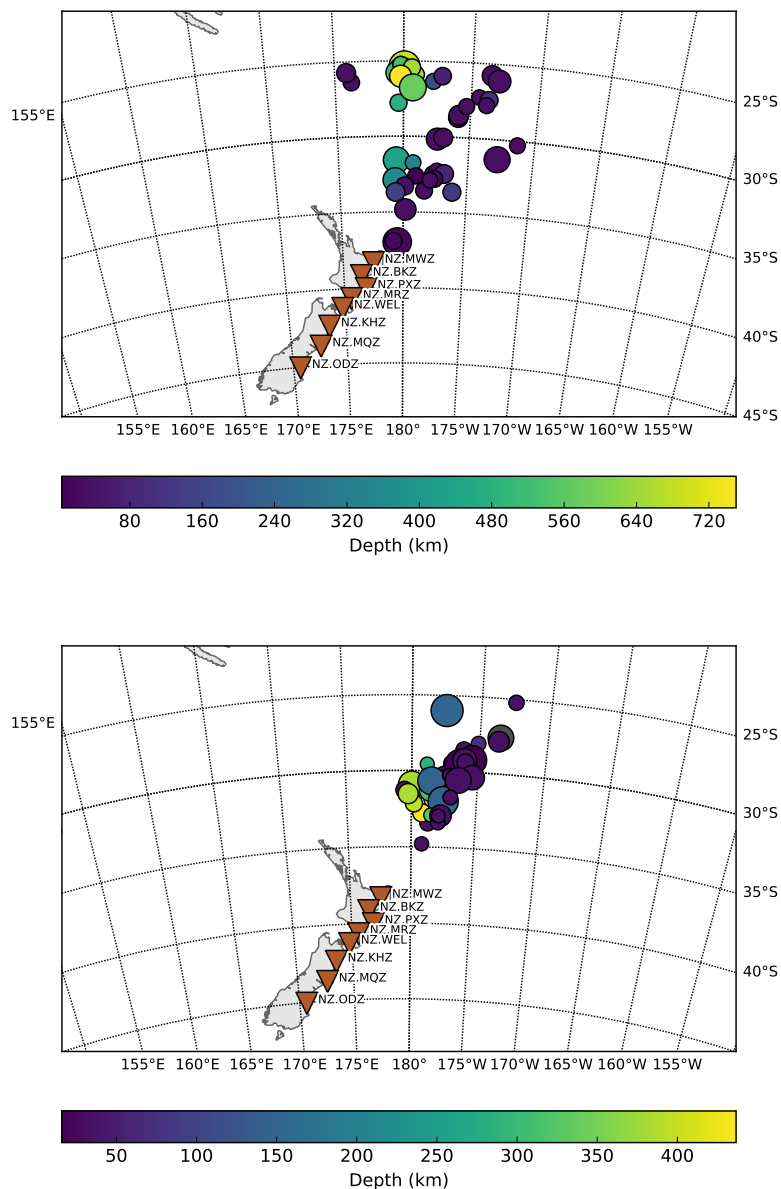


Figure 3.9: Maps of earthquake epicentres classified by the observation of a precursor signal. The upper map shows epicentres for which a high frequency precursor was not observed at any of the stations indicated, while the lower map shows the locations for which a precursor was observed in the seismogram of at least one station. The size of the circle indicates the relative magnitude above  $M_W 6.0$ .

To further explore the relationship between the observation of precursors and the epicentre location, a cross-plot of the total number of precursory signals observed for an event versus epicentre latitude was generated (Figure 3.10). Since the scatter is broadly spread in this plot, there does not appear to be a strong relationship between the total number of precursors observed and the latitude. However, Figure 3.10 does show that for the earthquakes generating at least one observable precursor, over half of the epicentres are located in a  $2^\circ$  region extending from  $29.5^\circ\text{S}$  to  $31.5^\circ\text{S}$ , including the three events for which precursory arrivals were observed at every station. It should also be noted apart from one of the 53 events, a precursor was observed at two or more stations for each event.

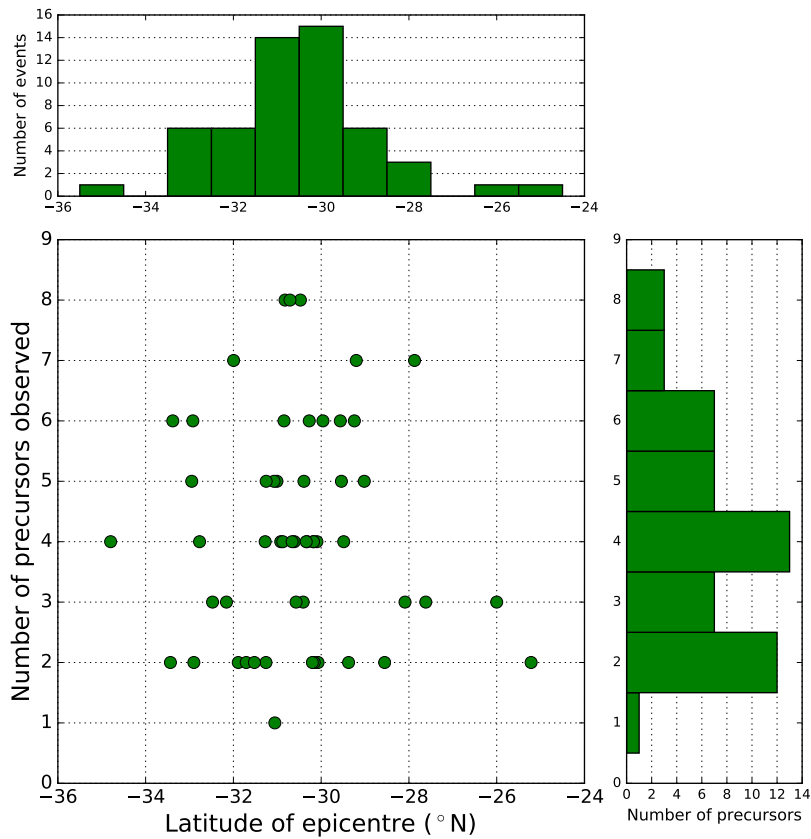


Figure 3.10: Total number of precursory signals observed versus epicentre latitude. The histograms show the total counts of the points along the respective axes.

The results thus far have demonstrated that the earthquakes generating observable leaky modes have hypocentres located close to the subducting slab within a specific range of latitudes. Another variable of interest in this multi-station analysis is the distance from the epicentre to the first station at which a precursor was observed, as this may give information concerning the distance over which a leaky mode must propagate in order to become distinguishable from lower frequencies.

Figure 3.11 shows a map relating the epicentre location to the closest station at which a precursor was observed. For the two events closest to New Zealand, a high frequency arrival is first observed at the more southern PXZ and MRZ stations, suggesting that a high-frequency precursor has not separated from lower frequencies at MWZ or BKZ (the closest event was the second event analysed in Section 3.2.1). However, for more distant epicentres, there does not appear to be a relationship between the latitude of the earthquake and the first station at which

a precursor is observed, evidenced by the spread of colours in the map. Moreover, the histogram in Figure 3.11 suggests there is not a strong relationship between the distance from an event to the station which first recorded a precursor, shown by the large spread of the station colour codes across the histogram. The peak in the data at 1000 km is most likely caused by more than half of the events occurring within a narrow  $2^\circ$  latitude range approximately 1000 km from MWZ. It should be noted that background noise which prevented an arrival from being observed does not affect this result, as noise prevented an observation of a precursor at a station further north than the location of the first observation of a precursor for only one event of the 53.

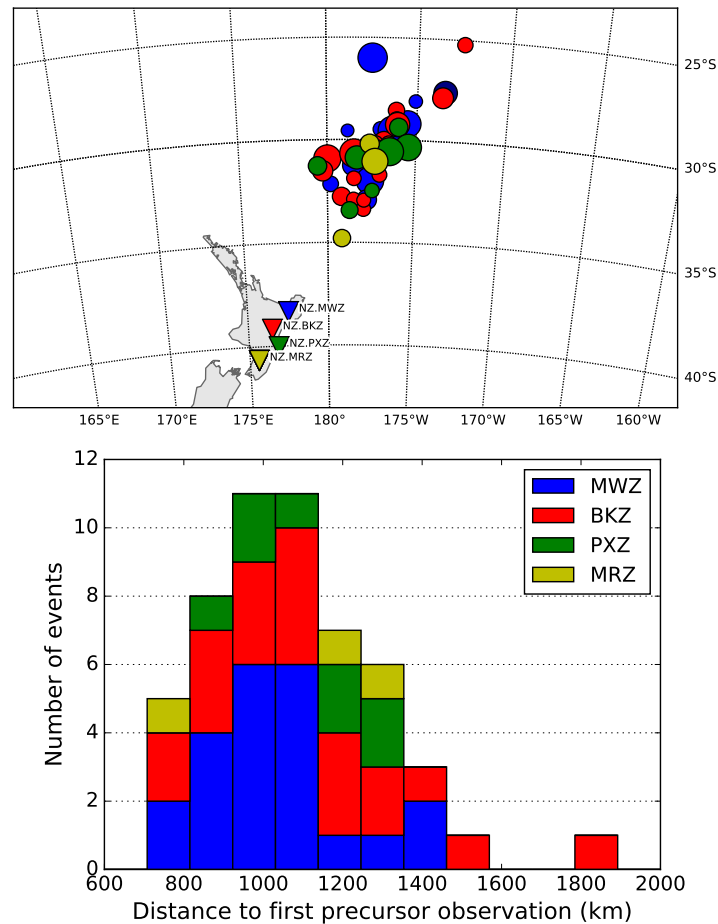


Figure 3.11: Relationship between epicentre locations and the closest station at which a precursor was observed. The top panel shows a map of epicentre locations colour coded based on the station at which a precursor was first observed. The histogram in the bottom panel shows the distributions of the distances between the epicentres and these stations.

### 3.3 Discussion

The results presented in the previous sections agree with the observations of previous studies (Ansell & Gubbins, 1986; Gubbins & Snieder, 1991; Smith et al., 1994; van der Hilst & Snieder, 1996). High-frequency precursors above 3 Hz are observed at New Zealand stations from earthquakes with hypocentres close to the subducting slab in the Kermadec region. Earthquakes producing these leaky modes occur in a region of latitude extending from  $25^\circ\text{S}$  to  $35^\circ\text{S}$ , with more than half of the epicentres located between  $29.5^\circ\text{S}$  and  $31.5^\circ\text{S}$ . Furthermore, the multi-station analysis of this study has shown that a large degree of variability is observed in

the frequency of occurrence of precursors at different stations in New Zealand. The epicentre latitude and the distance to the first observation of a precursory arrival have already been ruled out as significant factors influencing this variability. Several alternative explanations for the variability of precursor observations between stations are discussed here in order to relate the results of the multi-station analysis to the subsurface structure.

The first consideration is the ray paths of these earthquakes in relation to the high-velocity layer within the slab. Ansell and Gubbins (1986) demonstrate that the structure of the subducted slab to the north of New Zealand is curved such that the ray paths from the Kermadec events recorded in the North Island lie near to or within the slab for most of the propagation distance. They argue that the early arrivals originate only from earthquakes where the hypocentre-station geometry permits these rays to be recorded. van der Hilst and Snieder (1996) confirm this conclusion by analysing the intersection of the ray paths with the high velocity layer in the slab, concluding that high frequency arrivals are only observed when the ray path lies within the slab for the entire propagation distance. They did not observe precursors where the ray paths diverged from the subducted slab or reached into the lower mantle.

These conclusions may explain the variability in the observations of precursors at different stations. While the exact latitude of the epicentre is not an influencing factor, the location of the hypocentre with respect to the slab will influence the ray paths to the stations in New Zealand. It may be possible that a particular earthquake generates ray paths that follow the curvature of the high velocity layer over the entire propagation distance to some stations, while for other stations, the ray paths may diverge from the slab due to differences in the take-off angles or depths of the ray paths, preventing a leaky mode from being observed. Indeed, van der Hilst and Snieder (1996) conclude that the differences in precursor observations at SNZO near Wellington depend more on the location of the downgoing part of the ray in relation to the slab near the hypocentre than the location within the slab beneath the receiver.

Ray path considerations may offer an explanation as to why the most precursors are observed at MRZ in the lower North Island. The seismograph which Ansell and Gubbins (1986) use to demonstrate the alignment of the ray paths with the favourable curvature of the high velocity layer to produce very early precursory arrivals is MNG (Mangahao), a station located close to MRZ (Mangatainoka River) in the Wairarapa region. These observations suggest that the geometry of the slab and high velocity layer allow high-frequency leaky modes to be efficiently guided towards the lower North Island.

Further insight into the relationship between the position of the slab and the location of the stations is gained by examining the P-wave velocity at different depths beneath New Zealand. Figure 3.12 shows depth slices of the 3-D P-wave velocity model presented in (Eberhart-Phillips et al., 2010), which is a collation of several local tomographic 3-D seismic velocity models of New Zealand. Five depth slices have been taken at approximately 15 km intervals, revealing the approximate location of the subducted Hikurangi Plateau, visible as the linear high velocity feature extending down the East Coast of the North Island. While the resolution of this model is poor offshore towards the northeast of the North Island (Eberhart-Phillips et al., 2010), the highest velocities within New Zealand are beneath the lower North Island, as seen in the 35 km, 49 km, and 64 km depth slices. Moreover, it appears that the strike of the subducting slab is such that the stations towards the lower North Island are closer to the shallower parts of the slab than the northernmost stations. Notice also that the highest velocities only continue into the northern part of the South Island.

The observations from the velocity model offer an additional explanation for the variability of the occurrence of precursors between stations. High velocities within the subducted Hikurangi Plateau beneath the lower North Island allow the high-frequency leaky modes to propagate within the slab for a greater distance before refracting from the high velocity layer compared to areas further north or south. This implies that the energy recorded at stations such as PXZ, MRZ, and WEL may have propagated for a greater distance in the high velocity layer, causing

greater dispersion of the high frequencies and less attenuation from propagation through the crust above the slab compared to the other stations (this is consistent with the early high frequencies in the spectrogram of MRZ for the first event in Section 3.2.1). The location of refraction from the slab of rays recorded at stations such as MWZ and those in the South Island are likely further away from the location of the station, leading to the high-frequency leaky modes being attenuated more often before reaching the station. This interpretation is similar to the suggestion Love et al. (2015) offer to explain the variable length of the precursors observed from earthquakes within New Zealand, whereby longer precursors are observed where the subduction interface is located at shallow depths beneath a station.

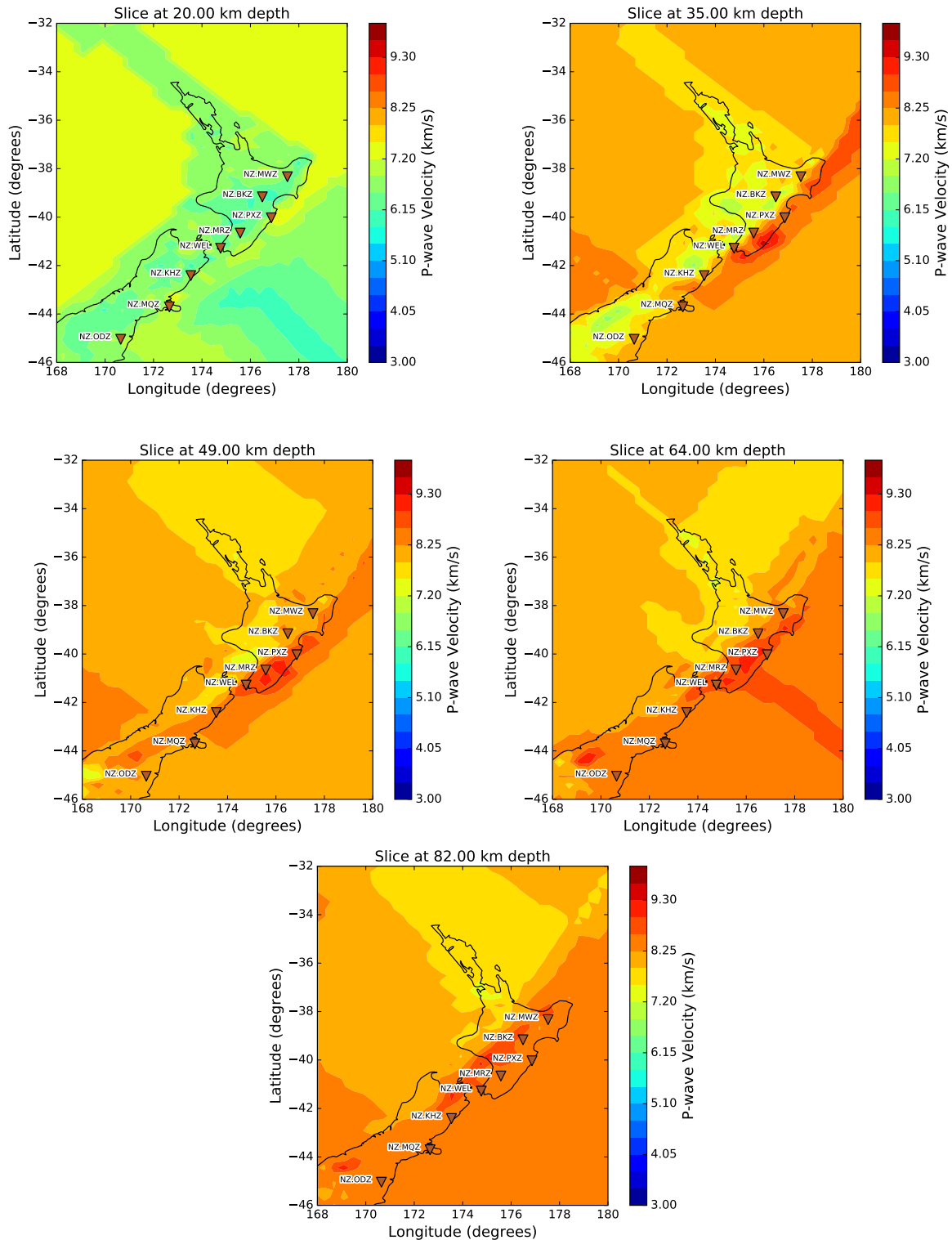


Figure 3.12: Depth slices of the New Zealand P-wave velocity model with station locations. The data are taken from the 3-D velocity model presented in Eberhart-Phillips et al. (2010).

## Chapter 4

# Conclusions

Leaky modes propagating as seismic waves through a high velocity layer in the subducted Pacific slab to the north of New Zealand are observed for earthquakes with hypocentres in the Kermadec region. These earthquakes, identified by the presence of high-frequency precursors above 3 Hz at seismometer stations in New Zealand, were observed to occur in a region extending from 25°S to 35° with hypocentres in close proximity to the subducting slab. Analyses of the waveforms and frequency content of the seismograms showed that high-frequency energy from the leaky modes arrived up to 10 s before lower frequency energy at stations in New Zealand, with narrow bands of frequency observed up to 9 Hz. These observations are consistent with those of previous studies.

An analysis of a catalogue of 97 earthquakes from the Kermadec region was performed to determine the frequency of occurrence of high-frequency precursors at eight digital seismometer stations down the East Coast of New Zealand. This analysis revealed that the most precursory arrivals were observed at a station in the lower North Island, and the least amount of arrivals were observed at stations in the South Island. Furthermore, no relationship was found between the latitude of the epicentre and the station where a precursor was first observed in New Zealand.

To explain the variability in the observation of precursors at different stations, the ray paths of the energy with respect to the high velocity layer in the slab were considered, along with the P-wave velocity structure in the Hikurangi subduction zone beneath New Zealand. This investigation showed that the likely causes for variability in the observation of precursors are the location of the ray paths through the high velocity layer in the slab, and the proximity of the shallow high velocities of the subducted slab to the stations at the surface. Leaky modes can propagate for greater distance through the high velocities beneath the lower North Island before refracting from the slab, while high frequency energy that must propagate to stations for significant distances outside the slab are attenuated to a greater degree, leading to less precursors being observed at these stations.

While this interpretation is consistent with results from previous studies using no more than two digital seismometers, further avenues of investigation are proposed below which would verify the interpretation and lead to information about the high velocity layer or crustal structure beneath the stations.

## 4.1 Future Work

Several areas are suggested for further investigation in order to validate the interpretation of the results of this study and further explore the phenomenon of leaky modes in the Kermadec subduction zone:

- An analysis of the waveforms and frequency content of each event in the catalogue could be performed at each station in order to gain information about the duration and frequency content of the precursors. This may lead to additional insight into the structure of the high velocity layer or the crust beneath the stations that leaky modes propagate through.
- For the two events analysed in Section 3.2.1, the difference in the focal mechanisms did not affect the observation of leaky modes. Studying the relationship between the observation of leaky modes and the focal mechanism of the earthquake (which may indicate the location of the hypocentre relative to the subducting slab) could give insight into the connection between the hypocentre parameters and the leaky modes.
- Ray paths from the events could be traced through a 3-D velocity model to all stations in order to verify the relationship between the observation of a precursor and the particular path that the energy follows to the stations.

## References

- Abers, G. A. (2000). Hydrated subducted crust at 100–250 km depth. *Earth and Planetary Science Letters*, *176*(3), 323–330.
- Abers, G. A., & Sarker, G. (1996). Dispersion of regional body waves at 100–150 km depth beneath Alaska: In situ constraints on metamorphism of subducted crust. *Geophysical Research Letters*, *23*(10), 1171–1174.
- Ansell, J., & Gubbins, D. (1986). Anomalous high-frequency wave propagation from the Tonga–Kermadec seismic zone to New Zealand. *Geophysical Journal International*, *85*(1), 93–106.
- Beyreuther, M., Barsch, R., Krischer, L., Megies, T., Behr, Y., & Wassermann, J. (2010). ObsPy: A Python toolbox for seismology. *Seismological Research Letters*, *81*(3), 530–533.
- Chen, K. H., Kennett, B. L., & Furumura, T. (2013). High-frequency waves guided by the subducted plates underneath Taiwan and their association with seismic intensity anomalies. *Journal of Geophysical Research: Solid Earth*, *118*(2), 665–680.
- Chiu, J.-M., Isacks, B. L., & Cardwell, R. K. (1985). Propagation of high-frequency seismic waves inside the subducted lithosphere from intermediate-depth earthquakes recorded in the Vanuatu Arc. *Journal of Geophysical Research: Solid Earth*, *90*(B14), 12741–12754.
- Eberhart-Phillips, D., & Reyners, M. (2012). Imaging the Hikurangi Plate interface region, with improved local-earthquake tomography. *Geophysical Journal International*, *190*(2), 1221–1242.
- Eberhart-Phillips, D., Reyners, M., Bannister, S., Chadwick, M., & Ellis, S. (2010). Establishing a versatile 3-D seismic velocity model for New Zealand. *Seismological Research Letters*, *81*(6), 992–1000.
- Furumura, T., & Kennett, B. (2005). Subduction zone guided waves and the heterogeneity structure of the subducted plate: Intensity anomalies in northern Japan. *Journal of Geophysical Research: Solid Earth*, *110*(B10).
- Gubbins, D., Barnicoat, A., & Cann, J. (1994). Seismological constraints on the gabbro-eclogite transition in subducted oceanic crust. *Earth and Planetary Science Letters*, *122*(1-2), 89–101.
- Gubbins, D., & Snieder, R. (1991). Dispersion of P waves in subducted lithosphere: Evidence for an eclogite layer. *Journal of Geophysical Research: Solid Earth*, *96*(B4), 6321–6333.
- Hunter, J. D. (2007). Matplotlib: A 2d graphics environment. *Computing In Science & Engineering*, *9*(3), 90–95.
- Iidaka, T., & Mizoue, M. (1991). P-wave velocity structure inside the subducting Pacific plate beneath the Japan region. *Physics of the Earth and Planetary Interiors*, *66*(3-4), 203–213.
- Kennett, B., & Engdahl, E. (1991). Traveltimes for global earthquake location and phase identification. *Geophysical Journal International*, *105*(2), 429–465.
- Krischer, L., Megies, T., Barsch, R., Beyreuther, M., Lecocq, T., Caudron, C., & Wassermann, J. (2015). ObsPy: A bridge for seismology into the scientific Python ecosystem. *Computational Science & Discovery*, *8*(1), 014003.
- Love, H., LeGood, M., Stuart, G., Reyners, M., Eberhart-Phillips, D., & Gubbins, D. (2015). Fast P-wave precursors in New Zealand: high velocity material associated with the subducted Hikurangi Plateau. *Geophysical Journal International*, *202*(2), 1223–1240.
- Martin, S., Rietbrock, A., Haberland, C., & Asch, G. (2003). Guided waves propagating in subducted oceanic crust. *Journal of Geophysical Research: Solid Earth*, *108*(B11).
- Percival, D. B., & Walden, A. T. (1993). *Spectral analysis for physical applications*. Cambridge University Press.
- Prieto, G. A., Parker, R. L., Thomson, D. J., Vernon, F. L., & Graham, R. L. (2007). Reducing

- the bias of multitaper spectrum estimates. *Geophysical Journal International*, 171(3), 1269–1281.
- Prieto, G. A., Parker, R. L., & Vernon, F. L. (2009). A Fortran 90 library for multitaper spectrum analysis. *Computers & Geosciences*, 35(8), 1701–1710.
- Prieto, G. A., Vernon, F. L., Masters, G., & Thomson, D. J. (2005). Multitaper Wigner-Ville spectrum for detecting dispersive signals from earthquake records. In *Signals, Systems and Computers, 2005. Conference Record of the Thirty-Ninth Asilomar Conference on* (pp. 938–941).
- Smith, G., Gubbins, D., & Mao, W. (1994). Fast P wave propagation in subducted Pacific lithosphere: refraction from the plate. *Journal of Geophysical Research: Solid Earth*, 99(B12), 23787–23800.
- Snieder, R., & van Wijk, K. (2015). *A guided tour of mathematical methods for the physical sciences*. Cambridge University Press.
- van der Hilst, R., & Snieder, R. (1996). High-frequency precursors to P wave arrivals in New Zealand: Implications for slab structure. *Journal of Geophysical Research: Solid Earth*, 101(B4), 8473–8488.

## Appendix A

# Determining Appropriate Spectrogram Parameters

A disadvantage of the multiple bandpass Wigner-Ville spectrogram in shown in Figure 3.3 is the tendency to under-emphasise the high frequency energy. The purpose of the bandpass filters applied to the seismograms in computing both of these time-frequency plots is to provide a means to equalise the seismic energy in each frequency range. This is necessary because the amplitude of the high frequency precursor is at least an order of magnitude less than the lower frequency main energy in all instances where significant dispersion is observed. However, even though the spectrograms in each frequency band were normalised, high energy contained in the low frequencies often caused a loss of contrast between the low energy precursor signal and the background noise when the spectrograms were plotted with a linear colour map. This is the reason why the seismogram of the replica in Figure 3.3 covers only 8 s as opposed to 12 s for the original plot, since the lower frequencies arriving between 8 s and 12 s overpowered the initial high frequency energy.

Separating the high frequency signal of interest from the low frequency energy proved to be a significant challenge toward studying the leaky modes using spectrograms. In an attempt to overcome this difficulty, spectrograms were displayed with a decibel colour scale to show detail over several orders of magnitude. Figure A.1 shows a comparison of a decibel scale plot alongside two alternative Wigner-Ville spectrograms. In order to remove high energy long wavelengths, the trace has been high-pass filtered at a frequency of 1 Hz, and the decibel scale is shown as decibels above the median value in order to enhance colour contrast. The linear colour scale is clearly inappropriate for studying the high frequency arrivals, as only the low frequency energy is visible. The multiple filters technique described above shows the high frequency onset at 6 Hz more clearly than the decibel scale plot, although the burst of energy at 3 Hz which is shown in the original figure (left panel of Figure 3.3) is visible in the decibel scale plot but not in the multiple filters plot. Since displaying the spectrogram with a decibel scale does not require significant modification of the trace through bandpass filtering, this method is deemed to be a more accurate representation of the true frequency content of the seismogram.

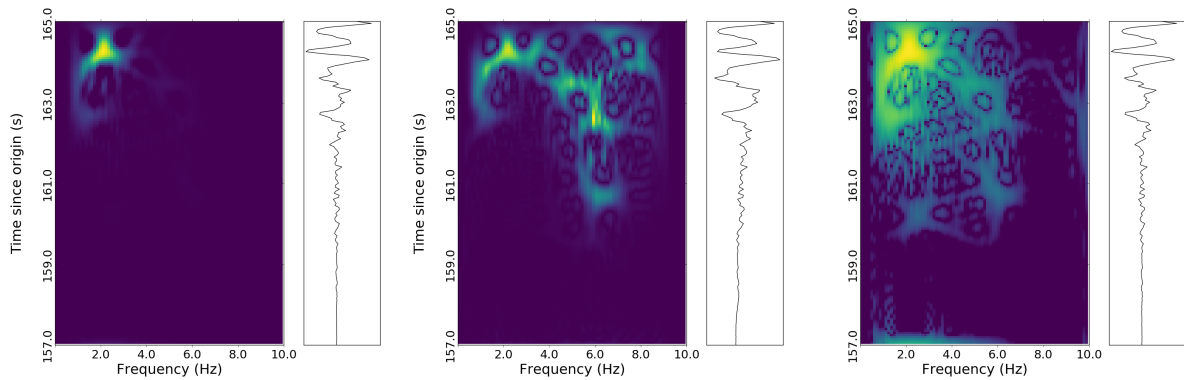


Figure A.1: Comparison of different spectrogram plotting methods. The left panel shows the Wigner-Ville spectrogram with a linear colour scale, the centre panel is the multiple bandpass filtered version (as in Figure 3.3), and the right panel is the Wigner-Ville spectrogram displayed with a decibel colour scale.

# Appendix A

## Multi-station Analysis Results

Table A.1 shows the precursor statuses for all events at multiple stations. The date and time of the earthquakes are given in UTC, magnitudes are  $M_W$  magnitudes, and the depths in are in km. For each station, a  $\checkmark$  indicates that high frequency precursor was distinguishable in the spectrogram, while a  $\times$  indicates that no high frequency precursor was observed. A  $-$  means that the signal was of poor quality or excessive noise masked the earthquake arrival (or in a few cases, no data was available).

Table A.1: Precursor statuses for all events (continues on next page)

Earthquake Parameters						Precursor Status							
Date	Time	Latitude	Longitude	Magnitude	Depth	MWZ	BKZ	PXZ	MRZ	WEL	KHZ	MQZ	ODZ
2014-06-23	19:19:13	-30.097	-176.794	6.6	30	$\times$	$\checkmark$	$\checkmark$	$\checkmark$	$-$	$\times$	$\checkmark$	$\times$
2015-08-09	04:46:20	-28.09	-175.095	6.1	72	$\checkmark$	$\checkmark$	$-$	$\checkmark$	$-$	$\times$	$-$	$-$
2013-12-03	21:05:31	-31.258	-177.593	6.1	337	$\checkmark$	$\times$	$\times$	$\checkmark$	$\times$	$\times$	$-$	$-$
2014-06-23	19:21:48	-30.156	-177.423	6.6	33	$-$	$-$	$-$	$-$	$-$	$\times$	$-$	$\times$
2009-11-22	22:47:27	-31.569	179.467	6.9	436	$\times$	$\times$	$\times$	$\times$	$\times$	$\times$	$\times$	$\times$
2014-06-23	22:15:44	-30.071	-176.395	6.0	33	$\checkmark$	$\checkmark$	$-$	$-$	$-$	$\times$	$\times$	$\times$
2016-02-01	19:00:45	-30.921	-179.985	7.2	382	$\times$	$\checkmark$	$\checkmark$	$\checkmark$	$\checkmark$	$\times$	$\times$	$\times$
2014-06-23	21:08:51	-30.159	-176.784	6.2	33	$\checkmark$	$\times$	$-$	$\checkmark$	$-$	$\times$	$\times$	$\times$
2016-09-24	04:02:14	-32.462	-177.72	6.1	33	$\times$	$\times$	$\times$	$\times$	$-$	$\times$	$\times$	$\times$
2016-06-06	02:35:24	-30.32	-177.438	6.5	0	$\times$	$\checkmark$	$\checkmark$	$\checkmark$	$-$	$\checkmark$	$\times$	$\times$
2016-08-12	03:29:28	-27.616	-173.488	7.1	0	$\checkmark$	$-$	$-$	$\checkmark$	$\checkmark$	$\times$	$\times$	$\times$
2013-07-19	11:40:42	-30.473	-176.286	6.6	22	$\checkmark$	$\checkmark$	$\checkmark$	$\checkmark$	$\checkmark$	$\checkmark$	$\checkmark$	$\checkmark$
2014-03-01	03:32:14	-31.741	-179.244	6.1	340	$\times$	$\times$	$\times$	$\times$	$\times$	$\times$	$\times$	$\times$
2013-07-03	15:09:02	-30.611	-178.107	6.0	62	$\checkmark$	$\checkmark$	$-$	$\checkmark$	$\checkmark$	$\times$	$\times$	$\times$
2012-02-26	05:24:57	-32.475	-177.433	6.0	33	$\times$	$\times$	$\checkmark$	$\checkmark$	$\checkmark$	$\times$	$\times$	$\times$
2014-03-19	16:00:19	-28.553	-176.143	6.3	33	$\times$	$\checkmark$	$\times$	$\checkmark$	$-$	$\times$	$\times$	$\times$
2016-11-12	16:15:57	-25.66	179.631	6.4	600	$\times$	$\times$	$\times$	$\times$	$\times$	$\times$	$\times$	$\times$
2011-10-21	17:57:16	-29.2	-175.5	7.4	16	$\checkmark$	$\checkmark$	$\checkmark$	$\checkmark$	$\checkmark$	$\checkmark$	$\checkmark$	$\times$
2014-07-18	18:23:04	-34.797	-179.165	6.1	33	$\times$	$\times$	$\times$	$\checkmark$	$\checkmark$	$\checkmark$	$\times$	$\checkmark$
2013-09-24	23:38:27	-25.778	-173.568	6.4	33	$-$	$-$	$-$	$-$	$-$	$-$	$-$	$-$
2014-06-23	22:20:05	-30.049	-176.973	6.3	33	$-$	$-$	$-$	$-$	$-$	$\times$	$\times$	$\times$
2008-03-28	06:39:47	-32.88	179.36	6.7	365	$\times$	$\times$	$\times$	$\times$	$-$	$\times$	$\times$	$\times$
2014-06-23	20:06:13	-29.96	-176.708	6.7	30	$\checkmark$	$\checkmark$	$\checkmark$	$\checkmark$	$-$	$\checkmark$	$\checkmark$	$\times$
2013-11-18	22:23:34	-31.009	-178.321	6.3	279	$\checkmark$	$\checkmark$	$\times$	$\checkmark$	$\checkmark$	$\checkmark$	$\times$	$\times$
2015-08-24	09:41:26	-30.875	-178.319	6.7	221	$\times$	$\times$	$\checkmark$	$\checkmark$	$\checkmark$	$\times$	$\checkmark$	$\times$
2012-01-07	18:38:08	-29.017	-176.108	6.3	31	$\times$	$\checkmark$	$\checkmark$	$\checkmark$	$\checkmark$	$\times$	$\checkmark$	$\times$
2015-05-25	10:01:54	-27.284	-174.412	6.0	33	$\times$	$\times$	$-$	$\times$	$-$	$\times$	$\times$	$\times$
2014-12-04	18:45:25	-27.42	-173.676	6.2	109	$\times$	$\times$	$-$	$\times$	$-$	$\times$	$-$	$\times$
2016-12-21	09:14:09	-31.889	-178.477	6.1	405	$\times$	$\checkmark$	$\times$	$\checkmark$	$\times$	$\times$	$\times$	$\times$
2009-02-18	21:53:31	-27.872	-173.612	6.6	33	$\times$	$\checkmark$						
2012-01-28	17:42:52	-29.486	-176.996	6.3	33	$\checkmark$	$\checkmark$	$\checkmark$	$\checkmark$	$-$	$\times$	$\times$	$\times$
2012-05-12	14:34:45	-25.216	-172.57	6.2	33	$\times$	$\checkmark$	$-$	$\checkmark$	$-$	$\times$	$\times$	$-$
2012-08-24	10:01:52	-33.435	-178.717	6.2	33	$\times$	$\times$	$\checkmark$	$\checkmark$	$\times$	$\times$	$\times$	$\times$
2014-01-10	02:22:51	-31.276	179.453	6.3	33	$\times$	$-$	$\checkmark$	$\checkmark$	$\checkmark$	$\checkmark$	$\times$	$\times$

Table A.1 continued

Date	Time	Latitude	Longitude	Magnitude	Depth	MWZ	BKZ	PXZ	MRZ	WEL	KHZ	MQZ	ODZ
2012-01-24	00:52:06	-25.361	-179.939	7.3	695	×	×	×	×	×	×	×	×
2013-02-24	20:54:02	-32.241	-177.395	6.0	33	×	×	–	×	–	×	–	×
2013-10-24	00:25:43	-31.074	-177.345	6.1	33	✓	✓	✓	✓	–	✓	×	×
2014-05-04	09:15:59	-25.595	179.873	6.8	551	×	×	×	×	×	×	×	×
2014-02-17	01:06:00	-30.179	-177.275	6.2	33	×	✓	×	✓	–	×	✓	✓
2013-02-18	16:32:40	-30.823	-177.143	6.2	33	✓	✓	✓	✓	✓	✓	✓	✓
2015-09-07	09:13:51	-33.626	-176.147	6.2	128	×	×	×	×	–	×	×	×
2013-07-03	20:13:31	-32.617	-179.021	6.1	5	×	×	×	×	×	×	–	–
2016-05-30	07:14:12	-30.411	-177.24	6.2	33	×	×	✓	✓	✓	×	×	×
2014-11-10	21:37:59	-30.201	-177.598	6.2	33	×	×	×	✓	–	✓	×	×
2016-03-29	11:03:06	-33.292	-179.89	6.2	33	×	×	×	×	×	×	×	×
2013-08-12	04:16:51	-31.253	-178.523	6.9	313	✓	✓	✓	✓	✓	×	×	×
2007-12-09	07:28:16	-26.0	-177.5	7.7	153	✓	✓	✓	×	–	×	×	×
2016-05-13	12:57:29	-25.899	-179.117	6.2	639	×	×	×	×	×	×	×	×
2016-09-01	16:37:55	-36.979	179.52	7.1	22	×	×	×	×	×	×	×	×
2014-11-04	18:21:12	-29.564	-178.843	6.1	286	✓	✓	×	✓	✓	✓	✓	–
2007-10-16	21:05:43	-25.775	179.53	6.6	509	×	×	×	×	–	×	×	×
2014-10-23	12:18:30	-33.574	-178.348	6.2	33	×	×	×	×	×	×	×	×
2013-09-30	05:55:50	-31.056	-177.287	6.7	33	×	×	×	✓	–	×	×	×
2015-06-25	18:45:53	-32.446	-176.812	6.3	85	×	×	–	×	–	×	×	×
2014-03-07	10:04:51	-28.695	-175.907	6.3	33	×	×	×	×	×	×	×	×
2012-10-19	15:34:07	-30.711	-176.385	6.4	33	✓	✓	✓	✓	✓	✓	✓	✓
2013-08-28	02:54:41	-27.783	179.633	6.2	478	×	×	×	×	×	×	×	×
2013-10-30	13:59:59	-25.226	179.799	6.1	526	–	–	–	×	–	×	–	–
2013-10-30	13:59:59	-25.226	179.799	6.1	526	×	×	×	×	–	×	×	×
2013-02-18	12:19:11	-30.846	-177.437	6.3	0	×	✓	✓	✓	✓	✓	✓	×
2014-09-10	16:32:04	-25.437	-179.395	6.2	643	×	×	×	×	×	×	×	×
2009-09-09	10:33:04	-32.771	-179.186	6.4	437	×	✓	✓	✓	✓	×	×	–
2013-06-10	06:26:23	-26.391	176.198	6.1	33	–	–	–	×	–	×	–	–
2017-01-29	14:59:44	-30.174	-176.532	6.1	30	×	✓	✓	✓	–	✓	×	×
2015-09-12	20:32:25	-32.793	-177.575	6.2	33	×	×	×	×	–	×	×	×
2011-07-06	19:03:18	-29.539	-176.34	7.6	17	✓	✓	✓	×	✓	×	✓	×
2016-06-23	07:44:30	-28.527	-175.87	6.4	33	–	–	–	–	–	×	–	×
2014-03-10	03:51:54	-25.739	175.843	6.3	33	–	–	–	×	–	×	×	–
2014-05-04	09:25:13	-26.017	179.782	6.6	750	×	×	×	×	×	×	×	×
2014-07-19	06:15:28	-32.158	-179.809	6.3	394	✓	✓	✓	×	×	×	×	×
2016-06-01	15:37:19	-30.393	-177.48	6.1	33	×	✓	✓	✓	–	×	✓	✓
2008-05-17	02:23:15	-33.684	179.394	6.3	146	×	×	×	×	–	×	×	×
2012-06-29	10:01:38	-27.787	-173.851	6.1	33	×	–	–	×	–	×	×	×
2015-09-07	14:06:26	-32.884	-177.895	6.0	33	×	×	×	×	–	×	–	–
2012-04-23	17:36:13	-29.243	-176.06	6.9	33	×	✓	✓	✓	✓	✓	✓	×
2013-10-11	21:25:00	-30.662	-178.484	7.3	151	×	✓	✓	×	✓	×	✓	×
2014-06-25	22:46:40	-30.272	-177.155	6.0	33	✓	✓	✓	✓	–	×	✓	✓
2006-05-16	10:39:14	-31.995	-177.556	7.5	152	✓	✓	✓	✓	–	✓	✓	✓
2013-09-01	19:50:43	-29.375	-175.994	6.3	33	×	×	✓	✓	×	×	×	×
2014-11-30	12:57:08	-32.901	-178.494	6.0	331	×	✓	×	✓	×	×	×	×
2016-09-01	17:14:05	-36.906	179.212	6.2	20	×	×	×	×	×	×	×	×
2014-02-02	09:26:37	-32.924	-177.733	6.7	33	✓	✓	×	✓	✓	✓	✓	×
2014-04-24	19:51:59	-26.127	-173.026	6.6	33	×	×	×	×	×	×	×	×
2014-10-14	04:12:30	-34.834	-179.823	6.5	33	×	×	×	×	×	×	×	×
2013-09-21	16:48:57	-33.381	-177.921	6.1	33	×	✓	✓	✓	–	✓	✓	✓
2016-07-05	19:06:46	-32.949	-177.902	6.0	33	×	✓	✓	✓	×	✓	✓	×
2014-03-26	03:29:40	-26.759	-179.324	7.0	577	×	×	×	×	×	×	×	×
2008-09-29	15:19:21	-30.341	-175.427	7.0	33	×	×	✓	✓	–	✓	✓	×
2014-03-26	04:23:19	-31.309	-172.775	6.9	33	×	×	×	×	×	×	–	–
2014-07-03	19:50:07	-30.572	-176.47	7.1	33	×	×	✓	✓	✓	×	×	×
2012-04-17	08:51:24	-31.708	-177.019	6.1	33	×	✓	–	✓	–	×	×	×
2012-08-24	04:43:50	-27.926	-175.318	6.1	33	×	×	–	×	–	×	×	×
2010-08-01	07:25:03	-31.522	179.741	6.6	385	×	✓	×	✓	×	×	×	×
2015-08-14	22:04:25	-26.334	-177.815	6.1	174	–	–	–	–	–	–	–	–
2013-10-29	08:21:53	-25.967	-177.162	6.2	71	–	–	–	–	–	–	–	–
2015-03-04	04:05:16	-30.282	-171.313	6.1	33	–	–	–	–	–	–	–	–
Total Number of Precursors:						22	39	34	48	24	21	22	10